

Multiscale Proper Orthogonal Decomposition (mPOD) of TR-PIV data— a Case Study on Stationary and Transient Cylinder Wake Flows

M A Mendez¹D Hess²B B Watz²J-M Buchlin¹¹von Karman Institute for Fluid Dynamics, Sint-Genesius-Rode, Belgium

mendez@vki.ac.be

²Dantec Dynamics AS, Denmark

Abstract

Data-driven decompositions of Particle Image Velocimetry (PIV) measurements are widely used for a variety of purposes, including the detection of coherent features (e.g., vortical structures), filtering operations (e.g., outlier removal or random noise mitigation), data reduction and compression. This work presents the application of a novel decomposition method, referred to as Multiscale Proper Orthogonal Decomposition (mPOD, Mendez *et al* 2019) to Time-Resolved PIV (TR-PIV) measurement. This method combines Multiresolution Analysis (MRA) and standard Proper Orthogonal Decomposition (POD) to achieve a compromise between decomposition convergence and spectral purity of the resulting modes. The selected test case is the flow past a cylinder in both stationary and transient conditions, producing a frequency-varying Karman vortex street. The results of the mPOD are compared to the standard POD, the Discrete Fourier Transform (DFT) and the Dynamic Mode Decomposition (DMD). The mPOD is evaluated in terms of decomposition convergence and time-frequency localization of its modes. The multiscale modal analysis allows for revealing beat phenomena in the stationary cylinder wake, due to the three-dimensional nature of the flow, and to correctly identify the transition from various stationary regimes in the transient test case.

Keywords: Data-Driven Modal Analysis, Multi-scale Proper Orthogonal Decomposition, Time-Resolved Particle Image Velocimetry, Transient Turbulent Cylinder Wake Flow, Time Dependent Vortex Shedding.

1 Introduction and Motivation

Data-driven decompositions of PIV measurements are nowadays part of the standard toolbox for post-processing techniques used to extract knowledge from data. Initially developed for identifying coherent structures in turbulent flows (Berkooz *et al.*, 1993, Lumley, 1970, Sirovich, 1987) and for reduced-order modeling (Holmes *et al.*, 1997, 1996), these decompositions have found applications also as random noise removal (Raiola *et al.*, 2015), image pre-processing tools (Mendez *et al.*, 2017) and for validation of numerical simulations (Erik *et al.*, 2007).

The scope of any decomposition is to describe the data as a linear combination of elementary portions referred to as *modes*. Each mode has its own spatial structure and temporal evolution and is potentially capable of describing essential features of the data. The removal of irrelevant modes enables filtering and data compression, while the dominant modes offer a basis for constructing reduced models capable of significantly reducing the computational burdens in the simulations of large dynamical systems. Modal decompositions and reduced-order models are

thus fundamentals in the development of control laws (Berger et al., 2014, Brunton and Noack, 2015).

Data-driven decompositions and modal analysis are reviewed by Amor et al. (2019), Benner et al. (2015), Rowley and Dawson (2017), Taira et al. (2017). The most common approaches can be broadly classified into two main classes: energy-based and frequency-based.

Energy-based decompositions arise from the Proper Orthogonal Decomposition (POD, Lumley (1970), Sirovich (1987, 1989)) and its variants. The POD provides the most energetic modes with no constraints on their frequency content. Variants of the POD can be constructed from different choices of the inner product or in the use of different averaging procedures in the computation of the data correlations. Examples of the first variants are proposed by Lumley and Poje (1997), Maurel et al. (2001), Rowley et al. (2004), where multiple quantities are involved in the inner product. Examples of the second variants are proposed by Citriniti and George (2000) and Towne et al. (2018), where the correlation matrix is computed in the frequency domain using time averaging over short windows, following the popular Welch’s periodogram method Welch (1967). The POD is known in other fields as Empirical Orthogonal Functions (EOF) decomposition or Principal Component Analysis (PCA). A review of these formulations in climatology is provided by Hannachi et al. (2007) and Ghil (2002).

Frequency-based methods arise from the assumption that a linear dynamical system can represent the dataset. The most common formulation in the fluid mechanics community is the Dynamic Mode Decomposition (DMD) introduced by Schmid (2010) and Rowley et al. (2009), although analogous formulations (see also Tu et al. 2014) were introduced in the late ’80s in climatology under the names of Principal Oscillation Patterns (POP, Hasselmann 1988, von Storch and Xu 1990) or Linear Inverse Modeling (LIM, Penland and Magorian 1993, Penland 1996). POP also inspired Oscillating Pattern Decomposition (OPD, Uruba 2012, 2015, Uruba and Procházka 2019) implemented in the Dantec software DynamicStudio (Ergin et al. 2014, Petersson et al. 2012).

Both constraints of energy optimality and spectral purity can become unnecessarily extreme, as discussed by Mendez et al. (2019). Energy-based methods fail to separate phenomena that occur at widely different frequencies (scales) and yet have comparable energetic contributions. Frequency-based methods face problems for datasets that are far from stationary and feature nonlinear phenomena such as frequency modulation, jitter, or impulsive events.

Significant effort has been placed in the development of hybrid methods, to complement the limitations of energy-based and frequency-based formulations, as recently discussed by Noack (2016). Examples of successful hybrid methods are the Spectral Proper Orthogonal Decomposition proposed by Sieber et al. (2016), the multiresolution Dynamic Mode Decomposition by Kutz et al. (2016), the Recursive Dynamic Mode Decomposition by (Noack et al., 2016) or Cronos-Koopman analysis by (Cammilleri et al., 2013). These methods propose ingenious combinations of POD and DMD and are designed for data sets that are statistically stationary (hinging on the time-frequency duality of the POD) or have short-duration departures from fixed points (hinging on the linearization of the dynamics in the DMD).

For datasets featuring transient evolution between different states and generally nonlinear dynamics, these methods lose their theoretical foundations and yield poor feature detection capabilities. The Multiscale Proper Orthogonal Decomposition (mPOD) proposed by Mendez et al. (2018b, 2019) is a hybrid decomposition that requires neither assumptions of stationary data nor linear dynamics. The mPOD combines Multi-resolution Analysis (MRA) via filter banks and standard POD to produce modes that are optimal within a certain range of frequencies (scales). A brief description of the decomposition is presented in Section 2.

The aim of this work is to test the mPOD on two challenging experimental test cases and compare it to classical energy-based and frequency-based tools. These investigated cases consist of Time-Resolved Particle Image Velocimetry (TR-PIV) of the turbulent flow past a cylinder in stationary and transient conditions, with varying free stream velocity and hence varying

frequency of the vortex shedding. While the stationary test case is one of the most classical paradigms for wake flows exhibiting large scale vortex shedding (see [Williamson \(1996\)](#) for a review), the transient configuration in turbulent conditions has received considerably less attention. Previous investigations on data-driven decomposition of the transient cylinder focus on the onset of the vortex shedding, both for reduced-order modeling ([Murata et al., 2019](#), [Noack et al., 2016, 2003](#), [Pawar et al., 2019](#), [Siegel et al., 2008](#)) and flow control applications ([Bergmann and Cordier, 2008](#), [Gronskis et al., 2009](#), [Rabault et al., 2019](#)).

It is worth highlighting that the cylinder wake flow at the Reynolds number investigated ($Re = [2600 - 4000]$) is inherently three-dimensional, characterized by the interaction of quasi two-dimensional structures with predominantly span-wise vorticity and longitudinal structures in the transverse plane (see [Chen et al. \(2017\)](#), [Hussain and Hayakawa \(1987\)](#), [Wu et al. \(1996\)](#)). A detailed experimental characterization of this interaction is out of the scope of this work (interested readers are referred to [Huang et al. \(2006\)](#), [Sung and Yoo \(2001\)](#), [Zhang et al. \(2000\)](#), [Zhou et al. \(2003\)](#)), which focuses on the assessment of the enhanced feature detection capabilities of the proposed mPOD.

The rest of the article is structured as follows. Section 2 briefly reviews the general formulation of energy-based and frequency-based methods, and introduces the mPOD. Section 3 presents the experimental setup and selected test cases, while Section 4 collects the results. Conclusions and perspectives are reported in Section 5.

2 Data-Driven Decompositions: POD, DMD/OPD and mPOD

The investigated dataset is a set of 2D velocity fields $\vec{u}(\mathbf{x}_i, t_k) = (\mathbf{u}(\mathbf{x}_i, t), \mathbf{v}(\mathbf{x}_i, t))$ over a uniform grid $\mathbf{x}_i \in \mathbb{R}^{n_x \times n_y}$, with i a matrix linear index, and a temporal discretization $t_k = \{(k-1)\Delta t\}_{k=1}^{k=n_t}$ with $\Delta t = 1/f_s$ the time step and f_s the sampling frequency. Bold fonts are used to indicate matrices.

All the analyzed data-driven decompositions break a discrete dataset into a linear combination of modes. These have a spatial structure $\vec{\phi}_k(\mathbf{x}_i)$, a temporal structure $\psi_r(t_k)$, and an amplitude σ_r . The sampled velocity field is thus expanded as

$$\vec{u}(\mathbf{x}_i, t_k) = \sum_{r=1}^R \sigma_r \vec{\phi}_r(\mathbf{x}_i) \psi_r(t_k) \quad (1)$$

A truncation of the summation to $\tilde{R} < \min(n_s, n_t)$ modes, assuming that these are sorted in descending order of energy contribution, defines the best \tilde{R} approximation of the data for a specific decomposition. The convergence of the decomposition as a function of the number of modes included can be monitored in terms of relative L_2 error in both space and time:

$$\mathcal{E}(\tilde{R}) = \frac{\|\vec{u}(\mathbf{x}_i, t_k) - \sum_{r=1}^{\tilde{R}} \sigma_r \vec{\phi}_r(\mathbf{x}_i) \psi_r(t_k)\|_2}{\|\vec{u}(\mathbf{x}_i, t_k)\|_2} \quad (2)$$

The decompositions used in this work, namely the POD, the DMD/OPD, and the mPOD are hereinafter distinguished using the subscripts \mathcal{P} , \mathcal{D} and \mathcal{M} respectively.

2.1 Energy-Based Formalism: the POD

The Proper Orthogonal Decomposition arises by minimizing the error in (2) $\forall \tilde{R} \in [1, R]$ or, equivalently, by maximizing the energy contribution of every mode. Both optimization problems are solved (see [Holmes et al. \(1997\)](#) or [Bishop \(2011\)](#)) in the framework of Principal Component Analysis, PCA) by taking the temporal structures as eigenvectors of the temporal correlation

matrix. This matrix is defined as $\mathbf{K}[k, n] = \langle \vec{\mathbf{u}}(\mathbf{x}_i, t_k), \vec{\mathbf{u}}(\mathbf{x}_i, t_n) \rangle_T$, with $\langle \bullet \rangle_T$ the inner product in the time domain. Hence, the temporal structures of the POD satisfy the eigenvalue problem

$$\mathbf{K} \psi_{\mathcal{P}r}(t_k) = \lambda_r \psi_{\mathcal{P}r}(t_k) \quad \forall r \in [1, R] \longrightarrow \mathbf{K} = \sum_{r=1}^R \lambda_r \psi_{\mathcal{P}r}(t_k) \psi_{\mathcal{P}r}^T(t_k) \quad (3)$$

having considered each temporal structure as a column vector, and having recalled, in the last summation, that the correlation matrix is symmetric and positive definite. The POD structures are, therefore, orthonormal.

Furthermore, one could show that $\lambda_r = \sigma_{\mathcal{P}r}^2$ and $\mathcal{E}(\tilde{R}) = \sigma_{\mathcal{P}_{\tilde{R}+1}}$. The normalization step in the calculation of the spatial structures in (1) is thus no longer necessary, and the corresponding spatial structures can be computed, hinging on the orthonormality of the temporal basis, using the inner product in the time domain, that is

$$\vec{\phi}_k(\mathbf{x}_i) = \frac{1}{\sigma_r} \left\langle \vec{\mathbf{u}}(\mathbf{x}_i, t_k), \psi_{\mathcal{P}r}(t_k) \right\rangle_T = \frac{1}{\sigma_r} \sum_{k=1}^{n_t} \vec{\mathbf{u}}(\mathbf{x}_i, t_k) \psi_{\mathcal{P}r}(t_k). \quad (4)$$

It is possible to show that these spatial structures are by construction also orthonormal and eigenvectors of the spatial correlation matrix $\mathbf{C}[i, n] = \langle \vec{\mathbf{u}}(\mathbf{x}_i, t_k), \vec{\mathbf{u}}(\mathbf{x}_n, t_k) \rangle_S$, with $\langle \bullet \rangle_S$ the inner product in the space domain. The computation of the POD modes from the eigenvalue decomposition of \mathbf{C} was originally presented by Lumley (1970) and is often referred to as *standard* POD. The computation of the spatial structures from the temporal ones via (3) and (4) was proposed by Sirovich (1987) and is often referred to as *snapshot* POD. The equivalence of the two approaches was first shown by Aubry et al. (1991).

If the Euclidian inner product is used in both space and time, the POD is equivalent to a Singular Value Decomposition (SVD) of the dataset matrix $\mathbf{D} = [d_1, d_2, \dots, d_{n_t}] \in \mathbb{R}^{n_s \times n_t}$, obtained by flattening each of the k snapshots into a column vector $d_k \in \mathbb{R}^{n_s \times 1}$. Here $n_s = 2n_x n_y$ denotes the dimension of the snapshot and the factor 2 accounts for the vector nature of the 2D velocity field. The SVD is thus introduced as $\mathbf{D} = \Phi_{\mathcal{P}} \Sigma_{\mathcal{P}} \Psi_{\mathcal{P}}^T$, where $\Phi_{\mathcal{P}} = [\phi_{\mathcal{P}1}[\mathbf{i}], \dots, \phi_{\mathcal{P}R}[\mathbf{i}]] \in \mathbb{R}^{n_s \times R}$ is the matrix of spatial structures, $\Sigma_{\mathcal{P}} = \text{diag}[\sigma_{\mathcal{P}1}, \dots, \sigma_{\mathcal{P}R}]$ is a diagonal matrix containing the amplitudes of each mode, and $\Psi_{\mathcal{P}} = [\psi_{\mathcal{P}}[k], \dots, \psi_{\mathcal{P}R}[k]] \in \mathbb{R}^{n_t \times R}$ is the matrix of temporal structures. In what follows, a tilde is used to denote basis matrices that are reduced, i.e. include only the columns corresponding to the first \tilde{R} dominant modes.

2.2 Frequency-Based Formalism: The DMD and the OPD

In the Dynamic Mode Decomposition (DMD) and the Oscillatory Pattern Decomposition (OPD), the temporal structures are complex exponentials with complex frequencies. The temporal structures are thus constructed as powers of a complex number $\lambda_r \in \mathbb{C}$. Starting the time discretization such that $t_0 = 0$ for $k = 1$, these structures can be written as follows:

$$\begin{aligned} \psi_{\mathcal{D}r}(t_k) &= \lambda_r^{k-1} = (|\lambda_r| e^{i\theta_r})^{(k-1)} = |\lambda_r|^{(k-1)} e^{i\theta_r(k-1)} = \\ &= |\lambda_r|^{(k-1)} e^{i2\pi f_r \Delta t (k-1)} = |\lambda_r|^{(k-1)} e^{i2\pi f_r t_k}, \end{aligned} \quad (5)$$

where $\theta_r = \arg(\lambda_r)$ is the argument of the complex number λ_r and the oscillation frequency associated to each mode is $f_r = \theta_r / (2\pi \Delta t)$.

In the Discrete Fourier Transform (DFT), the temporal basis is obtained by choosing the temporal structures as complex numbers of unitary modulus and frequency taken as multiple of a fundamental tone, that is $\psi_r[k] = \exp(i2\pi r \Delta f / f_s k)$ with $f_s = 1/\Delta t$ the sampling frequency. The classical DFT (see, for instance, Smith (2007)), the fundamental tone is taken as $\Delta f = 1/T$ with T the time span of the dataset. This is equivalent to assume periodicity of the data, and the resulting matrix of the temporal structure is the well known Fourier Matrix. The temporal

DFT is equivalent to the DMD based on the Companion matrix (see [Rowley et al. \(2009\)](#)) from which the temporal mean has been subtracted (see [Chen et al. \(2012\)](#)).

In DMD/OPD, aiming at approximating the dataset as a linear dynamical system, the complex numbers λ_r are eigenvalues of the propagator \mathbf{P} that advances one snapshot $\vec{\mathbf{u}}(\mathbf{x}_i, t_k)$ to the following –that is $\vec{\mathbf{u}}(\mathbf{x}_i, t_{k+1}) = \mathbf{P} \vec{\mathbf{u}}(\mathbf{x}_i, t_k)$. Flattening each snapshot into a column vector d_k , the linear dynamical system is defined as $d_{k+1} = \mathbf{P} d_k$, with the propagator being a square real matrix $\mathbf{P} \in \mathbb{R}^{n_s \times n_s}$.

Since the least square calculation of such propagator is computationally prohibitive in most real applications, the fitting of the linear dynamical system is carried out on a reduced space: the one spanned by the first \tilde{R} POD modes of the dataset. Splitting the dataset matrix into two shifted portions, that is $\mathbf{D}_1 = [d_1, \dots, d_{n_t-1}]$ and $\mathbf{D}_2 = [d_2, \dots, d_{n_t}]$, the propagator \mathbf{P} and its reduced counter part $\tilde{\mathbf{S}}$ are:

$$\mathbf{D}_2 = \mathbf{P} \mathbf{D}_1 \longrightarrow \underbrace{\tilde{\Phi}_P^T \mathbf{D}_2}_{\tilde{\mathbf{V}}_2} \approx \underbrace{\tilde{\Phi}_P^T \mathbf{P} \tilde{\Phi}_P}_{\tilde{\mathbf{S}}} \underbrace{\tilde{\Phi}_P^T \mathbf{D}_1}_{\tilde{\mathbf{V}}_1} \longrightarrow \tilde{\mathbf{V}}_2 \approx \tilde{\mathbf{S}} \tilde{\mathbf{V}}_1 \quad (6)$$

where the L_2 approximation lies in the second step, i.e. in the assumption that $\tilde{\Phi}_P \tilde{\Phi}_P^T \approx \mathbf{I}$ with \mathbf{I} the identity matrix of size $\tilde{R} \times \tilde{R}$.

The frequency-based formalism for data-driven decomposition is therefore based on the computation of the eigenvalues λ_r of the reduced propagator $\tilde{\mathbf{S}}$. In the classical DMD ([Schmid, 2010](#), [Tu et al., 2014](#)) this propagator is defined as follows:

$$\begin{aligned} \mathbf{D}_2 = \mathbf{P} \mathbf{D}_1 &\rightarrow \mathbf{P} \approx \mathbf{D}_2 \mathbf{D}_1^+ = \mathbf{D}_2 \tilde{\Psi}_P \tilde{\Sigma}_P^{-1} \tilde{\Phi}_P^T \\ &\rightarrow \tilde{\mathbf{S}} = \tilde{\Phi}_P^T \mathbf{P} \tilde{\Phi}_P = \tilde{\Phi}_P^T \mathbf{D}_2 \tilde{\Psi}_P \tilde{\Sigma}_P^{-1}, \end{aligned} \quad (7)$$

having introduced the Moore-Penrose inverse $\mathbf{D}_1^+ = \tilde{\Psi}_P \tilde{\Sigma}_P^{-1} \tilde{\Phi}_P^T$.

In the literature of Principal Oscillation Patterns (POP, [Hasselmann \(1988\)](#), [Penland \(1996\)](#), [von Storch and Xu \(1990\)](#)), the propagator is defined in terms of spatial covariance matrix $\mathbf{D}_1 \mathbf{D}_1^T$. Multiplying both sides by \mathbf{D}_1^T and inverting the spatial covariance matrix gives:

$$\mathbf{D}_2 = \mathbf{P} \mathbf{D}_1 \rightarrow \mathbf{D}_2 \mathbf{D}_1^T = \mathbf{P} \mathbf{D}_1 \mathbf{D}_1^T \implies \mathbf{P} \approx \mathbf{D}_2 \mathbf{D}_1^T (\mathbf{D}_1 \mathbf{D}_1^T)^{-1}. \quad (8)$$

2.3 The Multiscale Proper Orthogonal Decomposition (mPOD)

The Multiscale Proper Orthogonal Decomposition ([Mendez et al., 2018b, 2019](#)) presents a compromise between the POD and the DMD/OPD by adding spectral constraints to the energy optimality of the POD.

These constraints consist of breaking the datasets into the contributions of various scales using Multi-Resolution Analysis (MRA), as commonly proposed in Wavelet theory ([Mallat, 2009](#)), and in performing the POD for each scale.

A scale m corresponds to a range of frequencies, say $[f_{m1}, f_{m2}]$, identified by a transfer function, here indicated as a row vector $H_m \in \mathbb{C}^{1 \times n_t}$. This transfer function is ideally unitary (‘all pass’) within the range of interest and null (‘all stop’) otherwise. In the formulation presented in [Mendez et al. \(2018b\)](#), the transfer function of a given scale is applied in an equal manner to all the spatial realizations: to this end, the transfer function is copied row-wise in order to create a matrix of appropriate size $H'_m \in \mathbb{C}^{n_s \times n_t}$, later applied via direct matrix multiplication. Moreover, these transfer functions are taken as complementary, that is $\sum_m^M H'_m = \mathbf{1}$, and $H_i \odot H_j = 0 \forall i \neq j$, where $\mathbf{1} \in \mathbb{R}^{n_s \times n_t}$ is the unitary matrix (‘all-pass’) and \odot is the Schur (entry by entry) product.

The dataset decomposition into the contributions \mathbf{D}_m of M scales is:

$$\mathbf{D} = \sum_{m=1}^M \mathbf{D}_m = \sum_{m=1}^M \overbrace{\left[(\mathbf{D} \bar{\Psi}_{\mathcal{F}}) \odot \mathbf{H}'_m \right]}^{\hat{\mathbf{D}}_m} \Psi_{\mathcal{F}} \quad (9)$$

where $\Psi_{\mathcal{F}} \in \mathbb{C}^{n_t \times n_t}$ is the Fourier matrix $\Psi_{\mathcal{F}}[i, j] = \exp(2\pi j / n_t)^{(i-1) \times (j-1)}$, with $i, j = [1, n_t]$, the over bar denotes complex conjugation. Note that right multiplication by $\Psi_{\mathcal{F}}$ produce the row-wise Fourier transform of a matrix (i.e. in the time domain for \mathbf{D}) while multiplication by its conjugation (i.e. inverse. since $\Psi_{\mathcal{F}} \bar{\Psi}_{\mathcal{F}} = \mathbf{I}$) produce the row-wise inverse Fourier transform. The hat is used to denote the Fourier transform in time of the data ($\hat{\mathbf{D}} = \mathbf{D} \bar{\Psi}_{\mathcal{F}}$) and that of each contribution ($\hat{\mathbf{D}}_m = \mathbf{D}_m \bar{\Psi}_{\mathcal{F}}$).

Every contribution has its own POD, which could be used to construct suitable approximation of each scale:

$$\mathbf{D} = \sum_{m=1}^M \mathbf{D}_m = \sum_{m=1}^M \Phi_{\mathcal{P}}^{(m)} \Sigma_{\mathcal{P}}^{(m)} \Psi_{\mathcal{P}}^{(m)T} = \sum_{m=1}^M \mathbf{D}_m \Psi_{\mathcal{P}}^{(m)} \Psi_{\mathcal{P}}^{(m)T}. \quad (10)$$

The Multiscale POD is constructed by assembling the final mPOD temporal basis from all bases of all the scales. The mPOD algorithm saves computational time by operating the MRA on the correlation matrix and not on the dataset matrix- the equivalence between the two is revealed by introducing (9) in the definition $\mathbf{K} = \mathbf{D}_m^T \mathbf{D}_m$. In particular, the correlation matrix is split into the contribution of all the scales using an appropriate filter bank, i.e.:

$$\mathbf{K} = \sum_{m=1}^M \mathbf{K}^{(m)} = \sum_{m=1}^M \Psi_{\mathcal{F}} \left[\hat{\mathbf{K}} \odot \mathcal{H}_m \right] \Psi_{\mathcal{F}} = \sum_{m=1}^M \left(\sum_{r=1}^{n_m} \lambda_r^{(m)} \psi_{\mathcal{P}_r}^{(m)} \psi_{\mathcal{P}_r}^{(m)T} \right) \quad (11)$$

where $\hat{\mathbf{K}} = \bar{\Psi}_{\mathcal{F}} \mathbf{K} \bar{\Psi}_{\mathcal{F}}$ is the 2D Fourier transform of the correlation matrix, n_m the number of non-zero eigenvalues at each scale, and $\mathcal{H}_m = \mathbf{H}_m'^T \mathbf{H}_m'$ an appropriate 2D transfer function.

The eigenvalue decomposition of each contribution is introduced on the right-hand side of (11). The filters preserve the symmetry of the correlation matrices at each scale and hence the orthogonality of their eigenvectors. Moreover, avoiding frequency overlapping between different contributions to the correlation matrix, it is possible to keep the eigenvectors of different scales mutually orthogonal (see Mendez et al. (2019)) and hence orthogonal complements spanning the entire \mathbb{R}^{n_t} space (that is $\sum_{m=1}^M n_m \approx n_t$). This is achieved by constructing the 2D transfer functions, including only ‘pure’ terms, that is, the correlation of a transfer function with itself. In wavelet terminology, this corresponds to performing a Wavelet decomposition of the correlation matrix \mathbf{K} and retaining only the ‘approximation’ and ‘diagonal details’.

More information on the MRA formulation via dyadic wavelet decomposition is available in Mendez et al. (2018a,b). In this work, the MRA is performed using a generalized filter bank, as in Mendez et al. (2019), constructed using standard FIR filters designed via windowing method (?).

The resulting decomposition lets the mPOD recover the energy optimality of the POD at the limit of a single scale (spanning the entire frequency range), and the spectral purity of the DMD at the limit of n_t scales (each taking one frequency bin).

3 Experimental Set Up and Selected Test Case

The selected test case is the flow past a cylinder of $d = 5$ mm diameter and $L = 20\text{cm}$ length in transient conditions, with varying free stream velocity. The experiments were carried out in the L10 low-speed wind tunnel of the von Karman Institute, instrumented with a TR-PIV

system from Dantec Dynamics. The tunnel has a cross-section of $20\text{cm} \times 20\text{cm}$ and is equipped with a piezoresistive pressure transducer AMS5812 to monitor the pressure in the honeycomb chamber. A Laskin Nozzle PIVTEC45-M, operating with mineral oil Ondina Shell 91, is used to produce seeding particles of about $1.5\mu\text{m}$ in diameter, injected in the intake manifold of the wind tunnel fan.

The particles are illuminated with a Photonics Industries DM20-527DH Nd:YLF laser offering 20 mJ/pulse at 1 kHz . The exposed scene of about $70 \times 26\text{ mm}$ is recorded by a SpeedSense 9090 camera offering 7500 fps at a resolution of $1280 \times 800\text{ px}$. To extend the measurement duration, the sensor is cropped to $1280 \times 488\text{ px}$ resulting in a resolution of 18.3 px/mm and about $n_t = 13500$ double frames, sampled at a frequency of $f_s = 3\text{ kHz}$. At this frequency, the available light intensity is of the order of 6 mJ/pulse . The full dataset covers about 4.5 seconds. A picture of the experimental set-up is shown in Figure 1a).

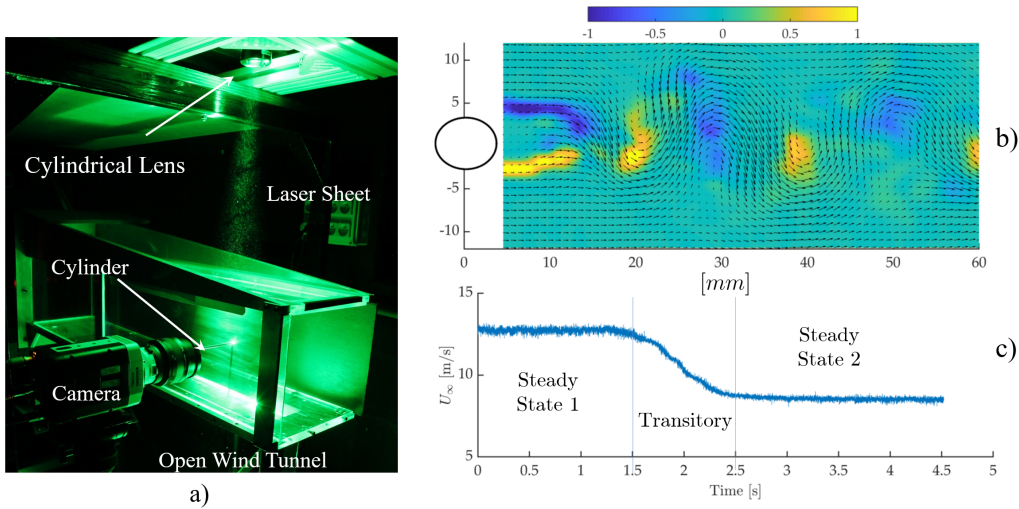


Figure 1: Fig a) Picture of the experimental set up during a TR-PIV measurement. Fig b) Instantaneous velocity field and normalized vorticity (that is scaled between $[-1, 1]$). Fig c) time evolution of the free stream velocity U_∞ , taken from a point far from the cylinder surface.

The DynamicStudio software is used for acquisition and analysis. For the initial data processing, standard adaptive PIV (see Theunissen (2010)) is used with an initial interrogation area of $96 \times 96\text{ px}$ and final size of $24 \times 24\text{ px}$, the vectors are calculated every 12 px resulting in an overlap of 50% . Before the mPOD analysis, the only filter applied is the universal outlier detection with a filter kernel of 3×3 vectors, as suggested by Westerweel and Scarano (2005).

An example of instantaneous velocity is shown in Figure 1b, together with the vorticity field normalized by the maximum and minimum values so as to have $\omega \in [-1, 1]$. In the investigated test case, the velocity of the free stream U_∞ evolves through two steady state conditions, namely from $U_\infty = 12.1 \pm 3\%$ to $U_\infty = 7.9 \pm 3\%$ m/s, as shown in Figure 1c). The transition between these is a smooth step of approximately 1 s . The Reynolds number varies from $Re \approx 4000$ to $Re = 2600$ and the frequency of the vortex shedding varies from 450 Hz to 303 Hz , corresponding to a Strouhal number of about $St = f d / U_\infty \approx 0.19$ in both stationary regimes. The entire range of Reynolds number experienced during the test falls in the three-dimensional vortex shedding regime (see Williamson (1996)).

4 Results and Discussion

The analysis is divided into two parts: the stationary conditions and the transient conditions. In the stationary conditions, discussed in subsection 4.1, only the first portion of the dataset is

considered. Referring to Fig. 1c), this covers a duration of $[0, 1.33s]$ and consists of $n_t = 4000$ snapshots. Since the PIV acquisition starts several minutes after the wind-tunnel has reached its stationary regime, this configuration can be seen as a fully developed stationary test case. In the transient conditions, discussed in subsection 4.2, the full set of $n_t = 13500$ snapshots is considered in the decomposition.

4.1 Analysis of the Steady State Condition

The mean flow field $U = \langle \vec{u} \rangle$ and the root mean square field $u_{rms} = \sqrt{\langle u'^2 \rangle + \langle v'^2 \rangle}$, with (u', v') the mean subtracted velocity components, are shown in Figure 2(a) and Figure 2(b) respectively. The root-mean-square reaches a maximum of about $u_{rms} = 6.9m/s$ at approximately $16mm$ from the cylinder axis. The flow statistics being well developed, the time average is subtracted before performing all the decompositions.

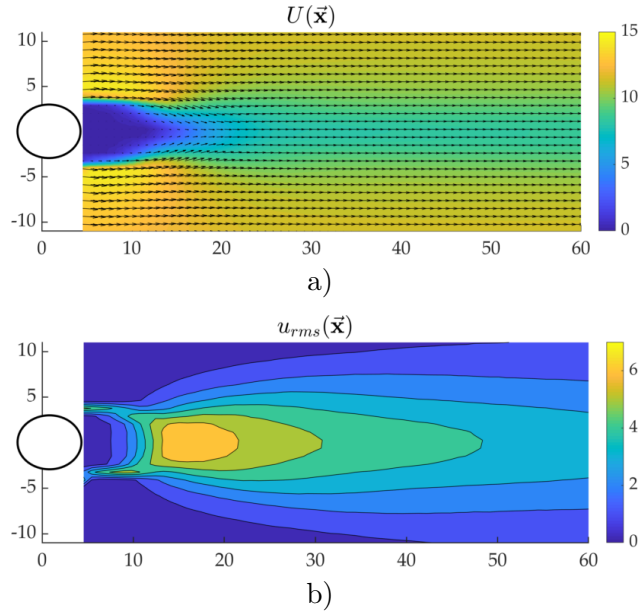


Figure 2: Mean velocity field (a) and root mean square (b) of the investigated test case. Both color-maps are in m/s while spatial units are in mm .

The key results from the DMD/OPD are collected in Figure 3. Figure 3a) shows the eigenvalue spectrum from the DMD/OPD, while 3b) and 3c) show the real and the imaginary part of the spatial structure associated with the dominant DMD/OPD mode. As stated earlier, no appreciable difference is observed between the propagators in (7) and (8), and hence only the results from the first are shown.

The plot of the eigenvalue spectra is shown in terms of modulus of the reduced propagator's eigenvalue \tilde{S} versus the associated frequency (only $f_n \geq 0$ are shown). The spectra is constructed for two choices of reduced POD basis, namely including $\tilde{R} = 10$ (red squares) or $\tilde{R} = 100$ POD modes (white circles) in (7) out of the $n_t = 4000$ available modes.

For both reduced POD bases, one eigenvalue with modulus $|\lambda_r| \approx 1$ is visible in the plots: this is linked to the dominant frequency in the flow produced by the vortex shedding. This eigenvalue, however, has a modulus slightly below unity ($|\lambda_r| = 0.9935$), possibly due to round-off errors, measurement noise, or insufficient sampling. As a result, this mode (as well as all the others) has a temporal structure that is exponentially decaying: the half-life of the dominant mode is of the order of 100 steps, i.e., about $3.3ms$, while all the other vanishes faster.

The energy associated with the DMD modes $\sigma_{D_r}^2$ is hence of little interest and not shown. As discussed in Section 2.2, these are the correlation between the initial snapshot of the data

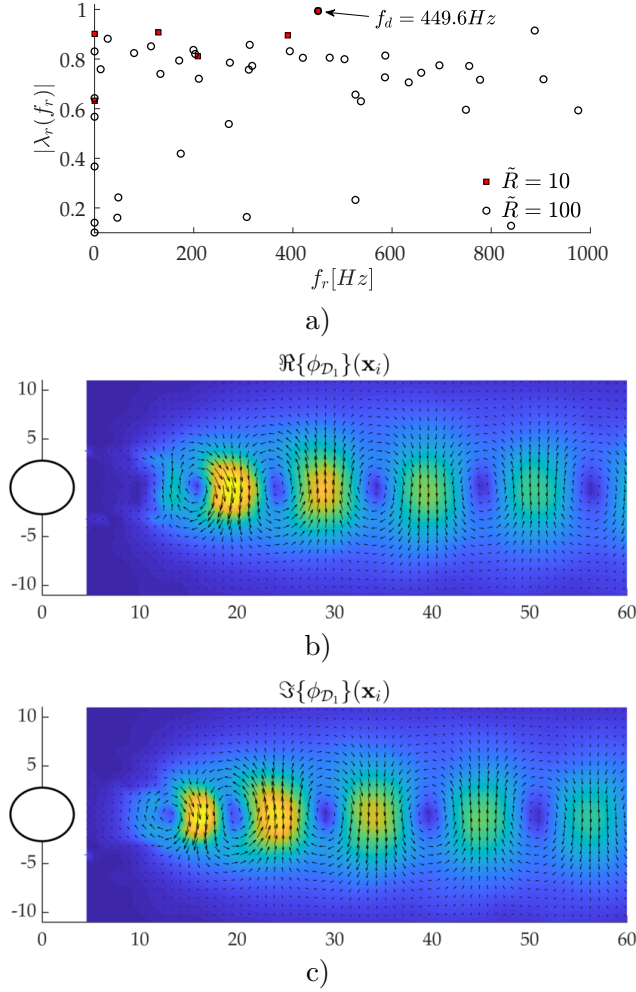


Figure 3: (a) Eigenvalue spectra from the DMD analysis in the stationary conditions with $U_\infty = 12.1m/s$. The real and the imaginary parts of the spatial structure associated to the dominant ($|\lambda_r| \approx 1$) mode, with frequency $f_d = 449.6Hz$, are shown in (b) and (c) respectively. Spatial units are in mm.

and the computed spatial basis, but the vanishing nature of the modes and the normalization of temporal and spatial structures make them unrepresentative of their relative importance.

The major limitation of the DMD is thus convergence: regardless of the size of the reduced POD basis, the vanishing of the modes make the error in (2) of the order of 95% even if all the modes of the decomposition are included.

The spatial structure associated with the dominant DMD modes in Figure 3b)-c) features a periodic pattern with a stream-wise wavelength of the order of the cylinder diameter. The first large vortical structure of the wake is centered at a distance of $\approx 16mm$ from the cylinder. Real and imaginary parts are phase-shifted in space, due to their harmonic ‘traveling wave’ nature.

In order to identify the structures associated with harmonic (i.e., not decaying) modes for these stationary test cases, the results of a DFT is also considered in Figure 4. Figure 4a) shows the energy contributions of the DFT modes as a function of their associated frequency (only $f_n > 0$ is shown) while Figures 4b)-c) show the real and the imaginary parts of the dominant mode. The energy spectrum is narrow and centered around the dominant frequency of the vortex shedding, labeled in the plot, and in agreement with the one identified by the DMD.

Although this mode is purely harmonic (with no decay), the real part of the spatial structures is similar to the DMD ones. The imaginary part, on the other hand, is not: while the classic overall spatial shift is also visible, the DFT mode displays a saddle point in place of the vortex

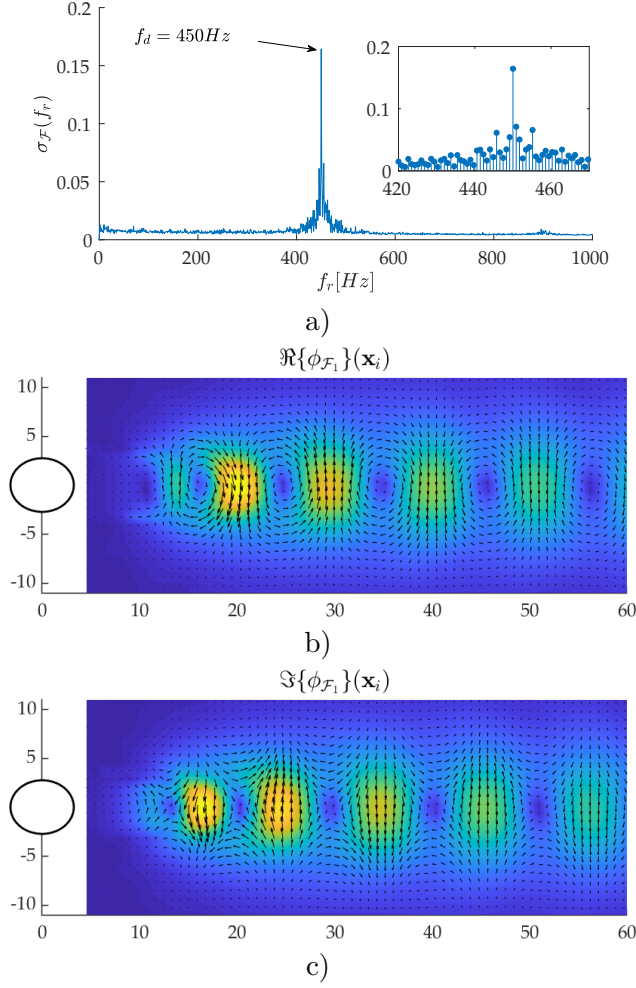


Figure 4: Spectra of the DFT amplitudes ($diag(\Sigma_{\mathcal{D}})$) the stationary test case with $U_{\infty} = 12.1m/s$. The dominant frequency of the vortex shedding is clearly visible. The real and the imaginary parts of the associated spatial structure are shown in b) and c) respectively.

core of the corresponding imaginary part in the DMD mode. Since the DMD and the DFT modes evolve at nearly the same frequency, this difference can only be due to their different duration: the saddle pattern appears as more representative of the flow evolution in the entire dataset while the structure identified by the DMD mode vanishes within 1/5 of the observation time. The flow topology of the saddle pattern is described by [Chen et al. \(2017\)](#), [Hussain and Hayakawa \(1987\)](#) as the result of the interaction between phase-shifted counter-rotating vortices produced in the von Karman street (see Fig. 15 in [Chen et al. \(2017\)](#)). This is also the region of larger strain and thus turbulence production; not surprisingly, the saddle point is located close to the region of larger root-mean-square velocity, as shown in Figure 2b).

To conclude the analysis of the stationary test case using state-of-the-art data-driven decomposition, the results for the POD, collected in Figure 5, are now considered. Figures 5a,b) show the spatial structure of the two dominant POD modes. These two modes are strongly linked, with nearly identical temporal evolution and frequency content. The time-frequency evolution of the first, using Continuous Wavelet Transform (CWT), is shown in 5c); the CWT of the second, being almost identical, is not shown. The CWT is performed using MATLAB's function CWT with a complex Morlet wavelet with bandwidth parameter $f_b = 5$ and center frequency $f_c = 1$ ([Misiti et al., 2015](#)) as a compromise between frequency and time resolution. The DFT of the associated temporal structures is shown in 5d), normalized with respect to the dominant frequency. Figure 5e) presents their phase portrait (Lissajous curves) produced by plotting one

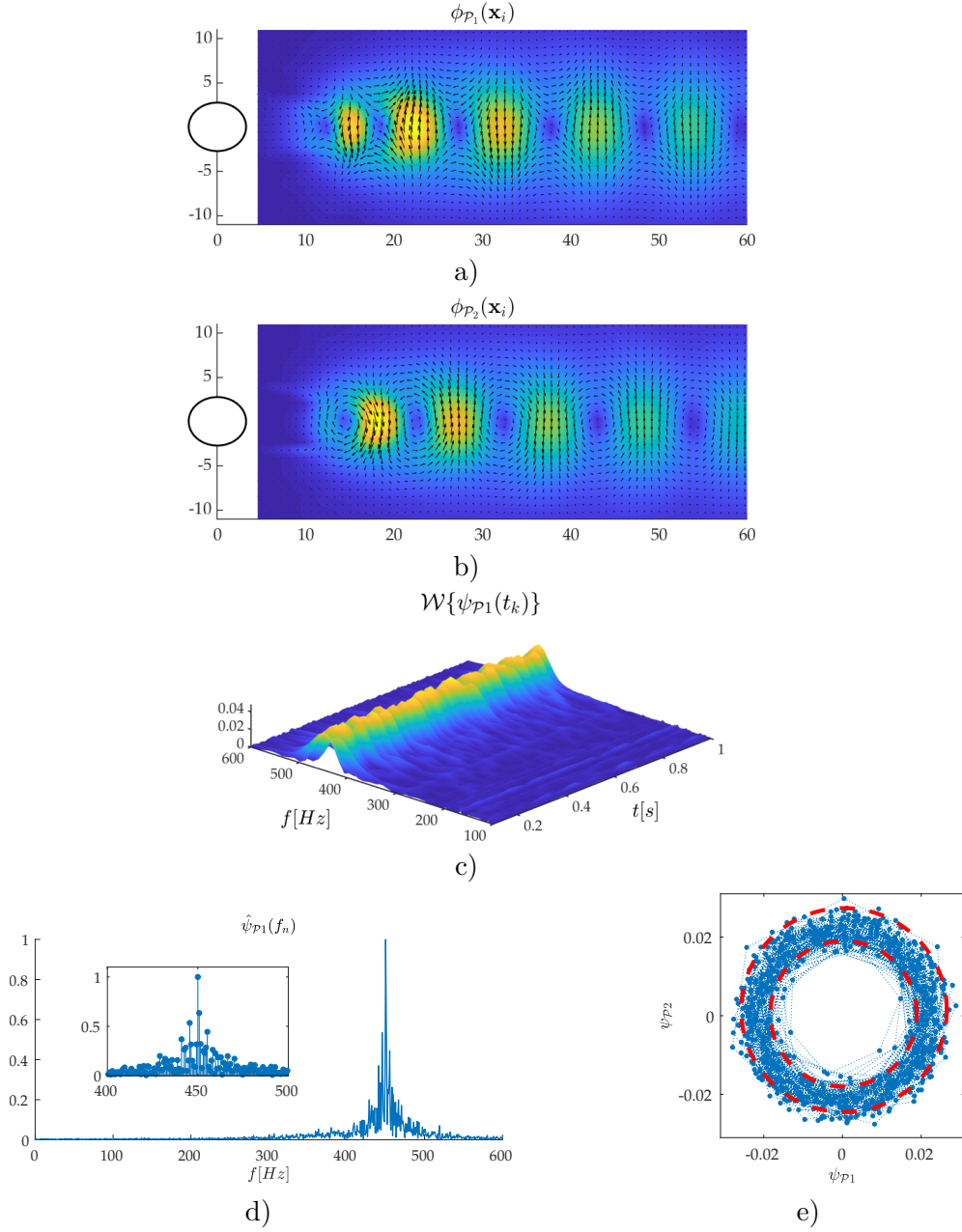


Figure 5: Results from the POD analysis of the stationary test case. The spatial structures of the dominant POD modes are shown in (a) and (b). Figure (c) shows amplitude of the CWT of the first temporal structure ψ_P , revealing the time-frequency evolution of these modes. Figure (d) shows their DFT. These modes have similar evolution, up to a $\pi/2$ phase difference, as shown by the phase portrait (Lissajous curve) in Figure (e).

temporal structure versus the other.

Since the POD modes are real, the traveling wave pattern is described by two modes in quadrature, which is clearly highlighted by the circular pattern produced by the Lissajous curve. The regularity of these patterns shows that the phase shift between the modes is overall time-invariant, similarly to what occurs in a DFT mode. As a result, the spatial structures of these two modes appear qualitatively similar to the real and the imaginary counter parts of the dominant DFT mode.

Nevertheless, the Lissajous curve shows a strong amplitude modulation, as the radius of the system trajectory varies in time between two extreme values, indicated in the figure with

dashed red lines. Since the frequency spectra of these modes appear time-invariant and narrow in the frequency domain, as shown by the CWT in 5c), this modulation can only be explained by two mechanisms: 1) the contribution due to phenomena having broad frequency spectrum (e.g. noise of turbulence) 2) the competition between harmonic modes having frequency close to the dominant shedding frequency.

The distinction between these two mechanisms cannot be revealed either by the DFT, because its harmonic modes do not admit modulation in time, neither by the POD, because its modes have too broad frequency content. In particular, it is interesting to observe that the DFT spectra of the temporal structures of the POD, shown in Figure 5d), is very similar to the DFT spectra of the entire dataset in Figure 4a). This is a direct consequence of the energy optimality, which allows these two POD modes to capture a significant amount of the dataset's energy, at the cost of mixing in the same modes a large range of scales. As shown by the stem plot zooming around the dominant peak, these modes have both contributions from frequencies close to the dominant one and larger tails of smaller amplitudes that extends over a frequency range of about $300Hz$. It is worth highlighting that the observation time covers about 5330 periods of the dominant frequency, and hence these secondary peaks are unlikely due to windowing phenomena (i.e., spectral leakage, see Harris (1978)).

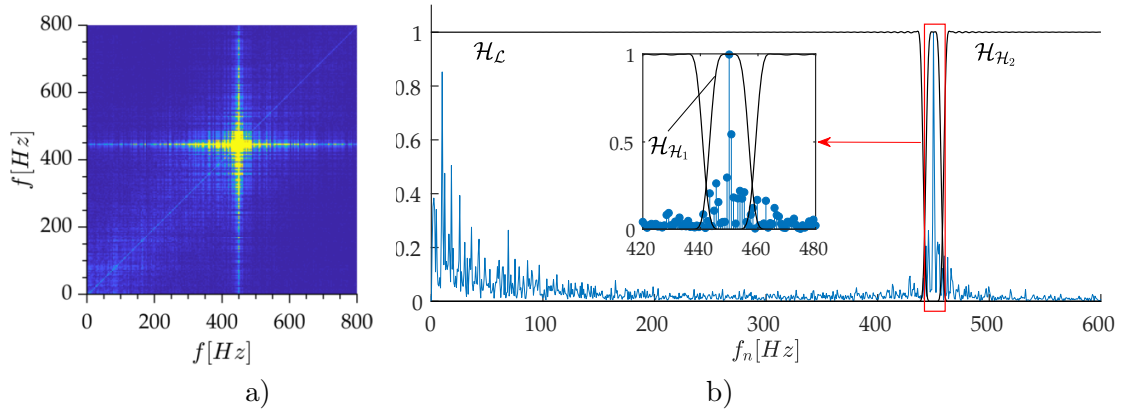


Figure 6: (a) Contour of the modulus of the Fourier transform of the correlation matrix \hat{K} and (b) auto-correlation spectra (i.e. diagonal of \hat{K}) with the modulus of the transfer functions of the selected scales ($diag(\Sigma_{\mathcal{D}})$).

The results from the mPOD are now discussed. For the purpose of this work and to illustrate the flexibility of this decomposition, it is interesting to obtain modes that have cleaner spectra than the POD ones in order to analyze the origin of the shedding modulation previously described. On the other hand, it is also of interest to achieve this without significantly compromising the convergence of the POD. To this end, only three scales are selected, starting from the one that should isolate the vortex shedding. The selection of the frequency range of each scale is illustrated in Figure 6 along with the auto-correlation spectra of the dataset (shown in 6b), that is the diagonal of the 2D Fourier transform of the correlation matrix \hat{K} (shown in 6a).

The correlation spectra show an important frequency content at a range $< 100Hz$; this is not visible in the first two dominant POD modes, but it is strongly present in the third and fourth POD modes (not shown). The scale centered around the vortex shedding is identified by a band-pass filter \mathcal{H}_1 with pass-band $f \in [445, 455]Hz$, while the other two scales take the remaining larger scales (filter $|\mathcal{H}_L| = 1$ in $f \approx [0, 445]Hz$) and finer scales (filter $|\mathcal{H}_2| = 1$ in $f \approx [455, 1500]Hz$). It is essential to observe that these spectral constraints only impose that a mode having frequency content in one scale does not have frequency content in others. Each scale is equipped with its POD, and the final mPOD basis is constructed by sorting these POD from various scales by energy contribution (associated eigenvalue).

All the filters are constructed using a windowing method with a Hamming window and

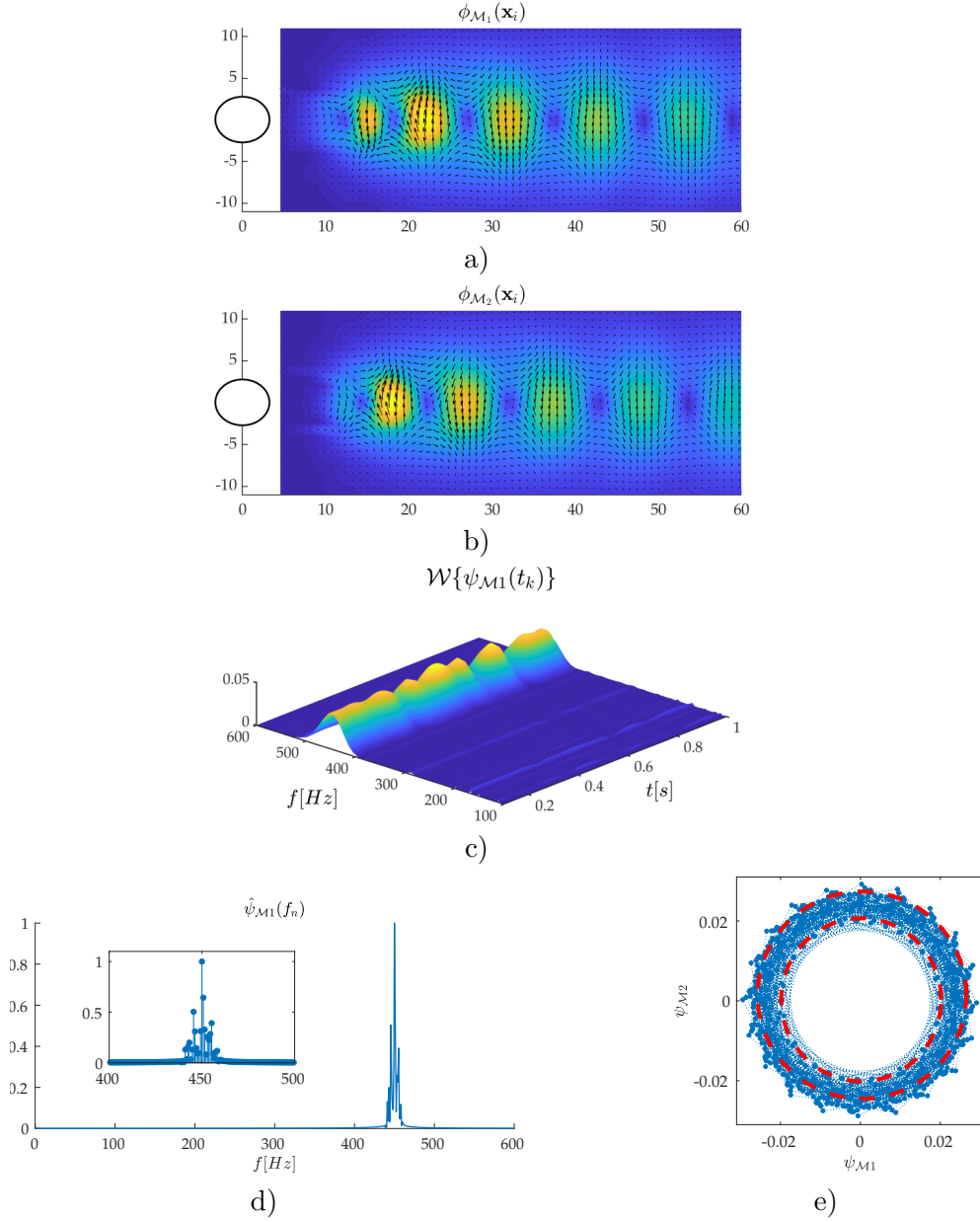


Figure 7: Same as Figure 5, but for the first two mPOD modes.

kernels of size $n_I = 2000$. The filtering is performed on the temporal correlation matrix using Matlab’s function `IMFILTER` with replicating boundary conditions (‘`REPLICATE`’ option). All the Matlab codes for the mPOD implementation are available online and described by [Ninni and Mendez \(2020\)](#).

The first two mPOD modes are shown in figure 7; the third and fourth are shown in figure 8. Both pairs share the same frequency spectra as for the POD pairs and the figures follow the same structure of figure 5.

The first mPOD pair of modes arise from the scale \mathcal{H}_1 , that is the one centered around the dominant vortex shedding frequency. The spatial structures of both modes feature the saddle region in the wake flow, and their CWT shows the modulation of their evolution in time. Because of their narrow frequency bandwidth, this modulation can only be linked to the interaction of different harmonic modes close to the shedding, which results in a beating phenomenon. This phenomenon is well described in standard textbooks on mechanical vibrations (e.g., [Rao \(2010\)](#)) and results from the interference of two harmonics motion having a similar frequency. The phase

portrait of these modes (Figure 7e) shows that the beating accounts for a significant portion of the modulation observed in the POD modes.

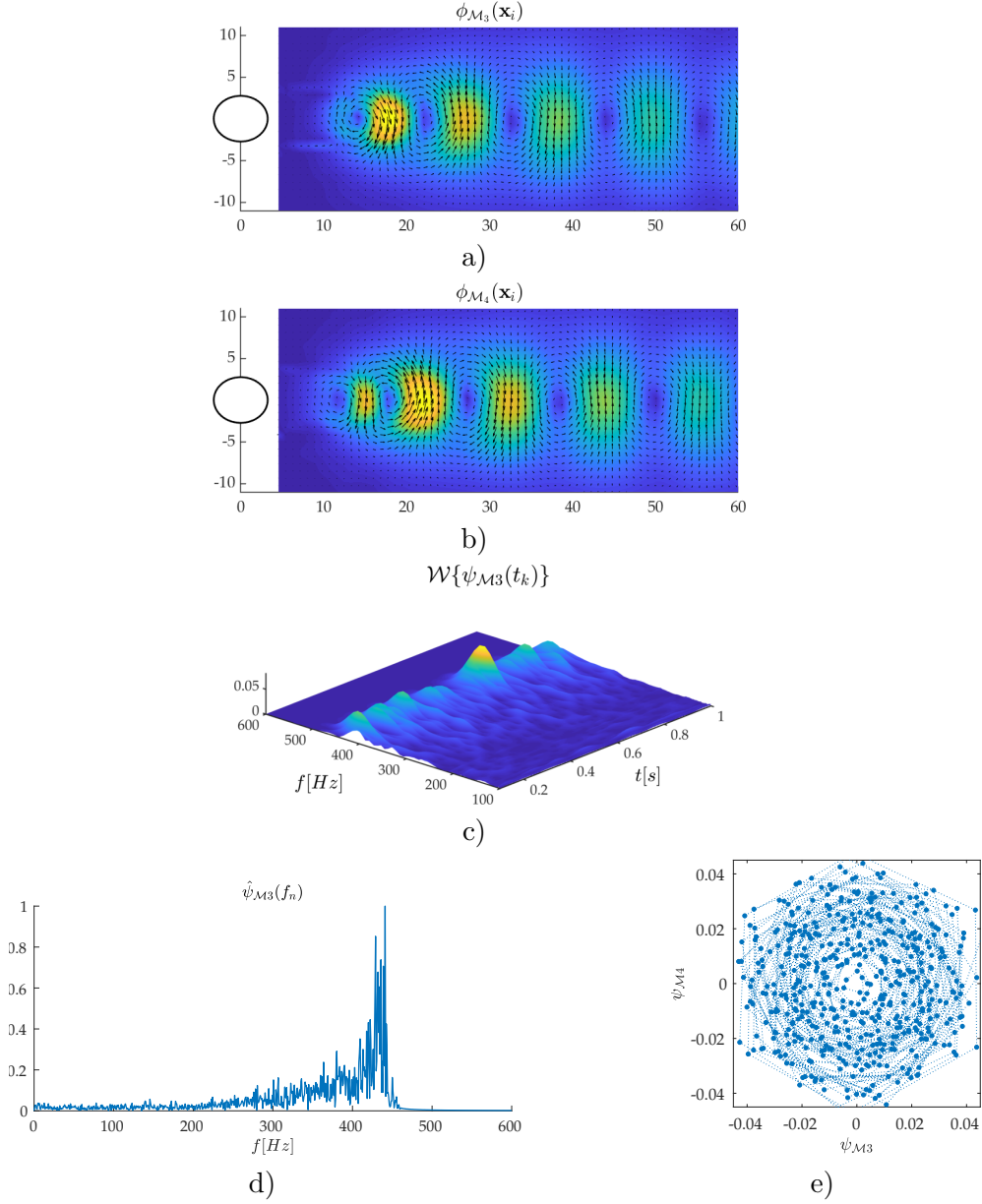


Figure 8: Same as Figure 5, but for the third and fourth mPOD modes.

The second mPOD pair of modes in Figure 8 arise from the large scale \mathcal{L} and is characterized by a frequency content which extends over the entire allowed spectra. A finer frequency selection could be used to reduce the frequency bandwidth of these modes, but for the purposes of this work it suffices to observe that these are not stationary: comparing the CWT transform of these modes in Figure 8c) with the one of the first two in Figure 7 shows that their contributions are complementary—the mode pair 3 – 4 is most active when the mode pair 1 – 2 is not. This intermittency results in the phase portraits that continuously spirals in and out (see Fig. 8e).

The spatial structures of these modes show the dominant vortical structure also observed in the harmonic decomposition. The mPOD describes, therefore, the dataset as a rather intermittent interplay of modes: the vortex shedding appears to slightly change its frequency content in time resulting in a temporal modulation and beating of the shedding amplitude mostly occurring at the dominant frequency detected by DFT and DMD. This intermittent effect is possibly

linked to the three-dimensional nature of the flow and particularly to the interaction between the quasi two dimensional Karman street with span-wise structures, that are characterized by similar frequency content (Zhang et al., 2000, Zhou et al., 2003).

Modes belonging to the highest frequency portion \mathcal{H}_2 have much lower energy and are not among the first ten mPOD modes– these are therefore not shown.

Finally, to conclude the analysis of the stationary test case, the decomposition convergence is discussed. Figure 9 shows the L_2 error over the full dataset (in this case, the first $n_t = 4000$ snapshots) as a function of the number of modes used in the approximation. The convergence results of the DMD/OPD are not shown since this decomposition does not converge to the dataset. While the spectral constraints in the mPOD do not allow to reach the optimal convergence of the POD, the two decompositions reach comparable convergence for $\tilde{R} > 8$. In particular, it appears that the information contained in the first five POD modes (producing $\mathcal{E} = 0.204$) is distributed to the first six mPOD modes (producing $\mathcal{E} = 0.200$). This result shows that the mPOD allows for more degrees of freedom than the POD in the modal analysis while maintaining comparable convergence, contrary to harmonic methods. For comparison purposes, the plot also shows the convergence of the DFT in time, which is considerably poorer. This represents the limit at which the mPOD tend if the spectral constraints in the MRA are increased to the extreme of having only one harmonic per scale.

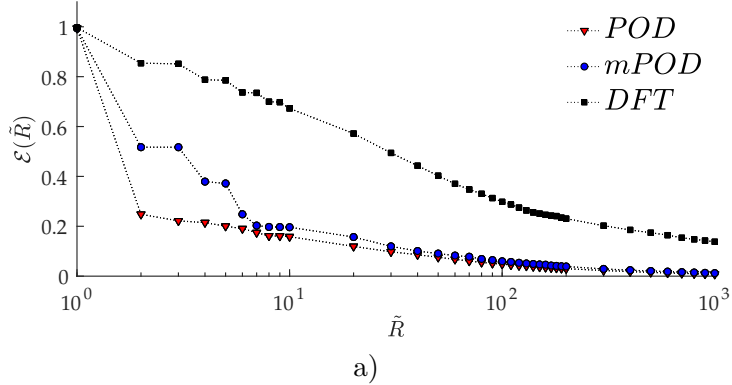


Figure 9: Decomposition error \mathcal{E} in (2) as a function of the number of modes included in the summation (1) for the POD, the mPOD and the DFT of the stationary dataset at $U_\infty = 12.1m/s$.

4.2 Analysis of the Transient Conditions

The full set of velocity fields is now considered, with free stream velocity evolving, as shown in Figure 1c. Since the flow is in transient conditions, the time-averaged flow is of little significance, and it is therefore not removed from the dataset before performing POD and mPOD. For the DFT, the mean removal is only a matter of plotting purposes (since the mode at $f = 0$ is available on the basis), while for the DMD/OPD, the time-averaged flow removal turned out to have no impact on the presented results.

The eigenvalue spectra of the DMD/OPD with the same reduced propagator described in the previous case is shown in Figure 10. A dominant frequency of $f_d = 390.2Hz$ is observed. This is somewhere in between the one linked to the vortex shedding in the first ($f_d \approx 450Hz$) and the second ($f_d \approx 303Hz$) stationary conditions. As for the previous case, this decomposition does not converge to the dataset. The associated spatial structures are, therefore, not shown.

The results of the DFT are shown in Figure 11. Figure 11a) shows the energy distribution as a function of the associated frequency. The frequencies of the vortex shedding in the two stationary test cases are visible and labeled. Figures 11b) and 11c) shows the real parts of the spatial structures associated with the dominant frequencies in the two shedding regimes.

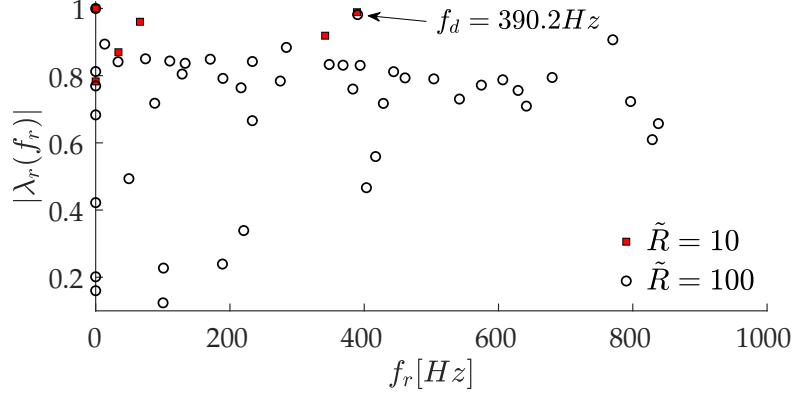


Figure 10: Eigenvalue spectra from the DMD analysis in of the full dataset (transient conditions). The computed dominant frequency is somewhere in between the two expected ones.

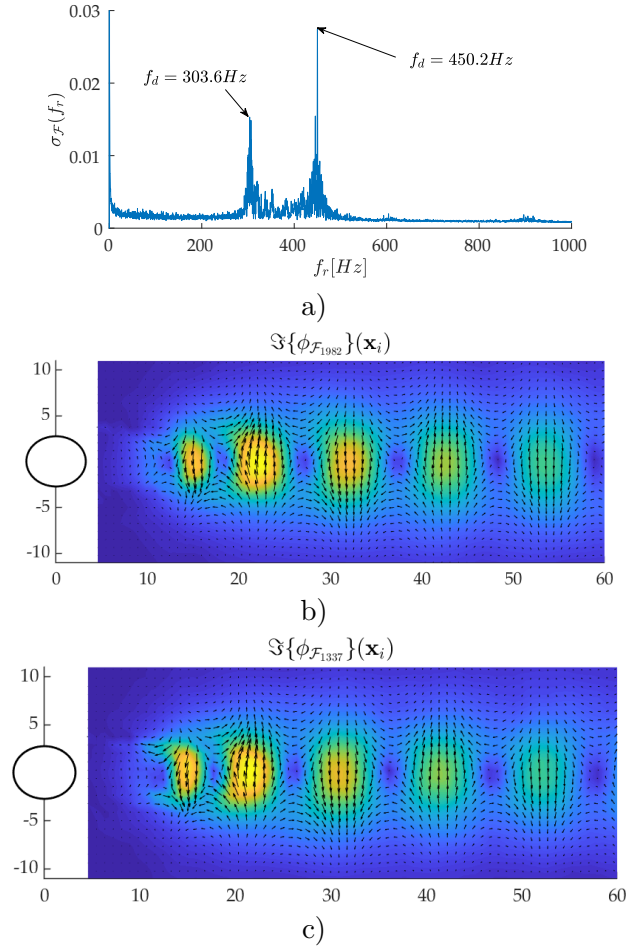


Figure 11: (a) Spectra of the DFT amplitudes ($diag(\Sigma_{\mathcal{D}})$) for the transient test case, showing the two harmonics dominating in the two stationary regimes. The imaginary part of the spatial structures associated to the frequency of the shedding at $U_{\infty} = 12.1m/s$ (that is $f_d = 450Hz$) is shown in (b) while the one associated to the frequency of the shedding at $U_{\infty} = 7.9m/s$ (that is $f_d = 303.6Hz$) is shown in (c).

These structures are similar: the first is associated with the stationary regime at $U_{\infty} = 12.1m/s$ while the second is linked to the stationary regime at $U_{\infty} = 7.9m/s$. The saddle pattern observed in the previous stationary test case is present in both, with a slight shift

linked to the different free stream velocity in which they become more representative. On the other hand, since these modes are purely harmonic, it is not possible to infer any temporal information regarding their occurrence. Moreover, since these modes are obtained by projecting the entire dataset onto harmonics that are mostly present in different time intervals, a distortion is produced in the spatial structures if compared to the ones obtained in an entirely stationary test case. This can be observed by comparing the imaginary part of the structure at Figure 11b) with the one in Figure 4c) where only the stationary case was considered.

The POD is now discussed. Since the temporal average is not removed, it is of interest to consider the first mode separately, which accounts for about 85.5% of decomposition convergence, i.e., $\mathcal{E}(1) = 15.5\%$ from (2). Its spatial and temporal structures are shown in Figure 12, and describe the large scale variation of the flow. In the general framework of a triple decomposition (Reynolds and Hussain, 1972), this mode could be seen as the base flow, i.e., the slowly varying contribution or ‘shift mode’ (Bourgeois et al., 2013, Noack et al., 2003, Tadmor et al., 2010). Nevertheless, since the POD sets no constraints on the frequency content of its modes, the temporal evolution exhibits additional higher frequencies.

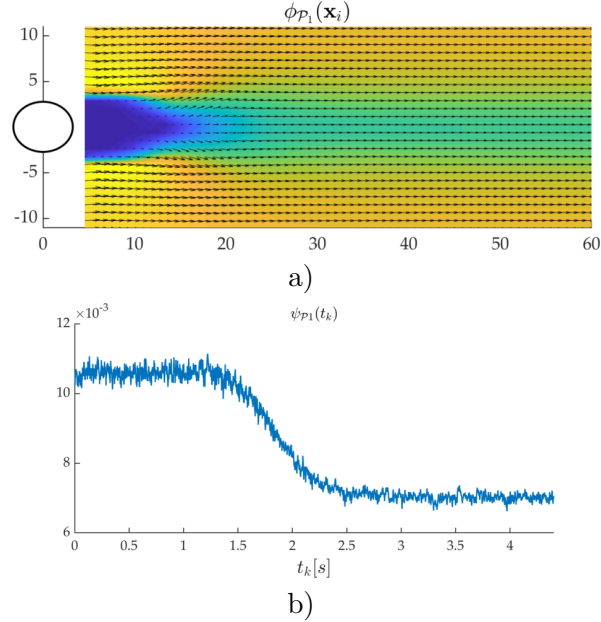


Figure 12: Spatial structure (a) and temporal structure (b) of the dominant POD mode for the transient test case.

The first pair of POD modes linked to the shedding frequencies (modes 2 and 3) are shown in Figure 13, following the same structure as Figure 5. These two POD modes account for an additional 11.54% of the decomposition convergence, and the error produced by an approximation including the first three POD modes is $\mathcal{E}(3) = 3.46\%$. These POD modes describe the evolution of the vortex shedding in the *entire* dataset, i.e., including both the stationary conditions and the transient. The CWT of their temporal structure shows how the frequency changes in time and evolves, interestingly, so as to keep the Strouhal number constant also during the transitory. The DFT of their temporal structure shows the two peaks and is, again, very close to the DFT of the entire dataset shown in Figure 11. As a result, the phase portrait is difficult to interpret, and so are the associated spatial structures that are, in fact, a combination of the ones to be expected for the different phases, namely from Figure 1c), the steady-state 1, the transitory, and the steady-state 2.

The results from the mPOD are now discussed. For the purpose of this test case, it is interesting to separate the modes that are associated with the two steady conditions and the ones associated with the transient. As with the previous test case, Figure 14a) shows the contour

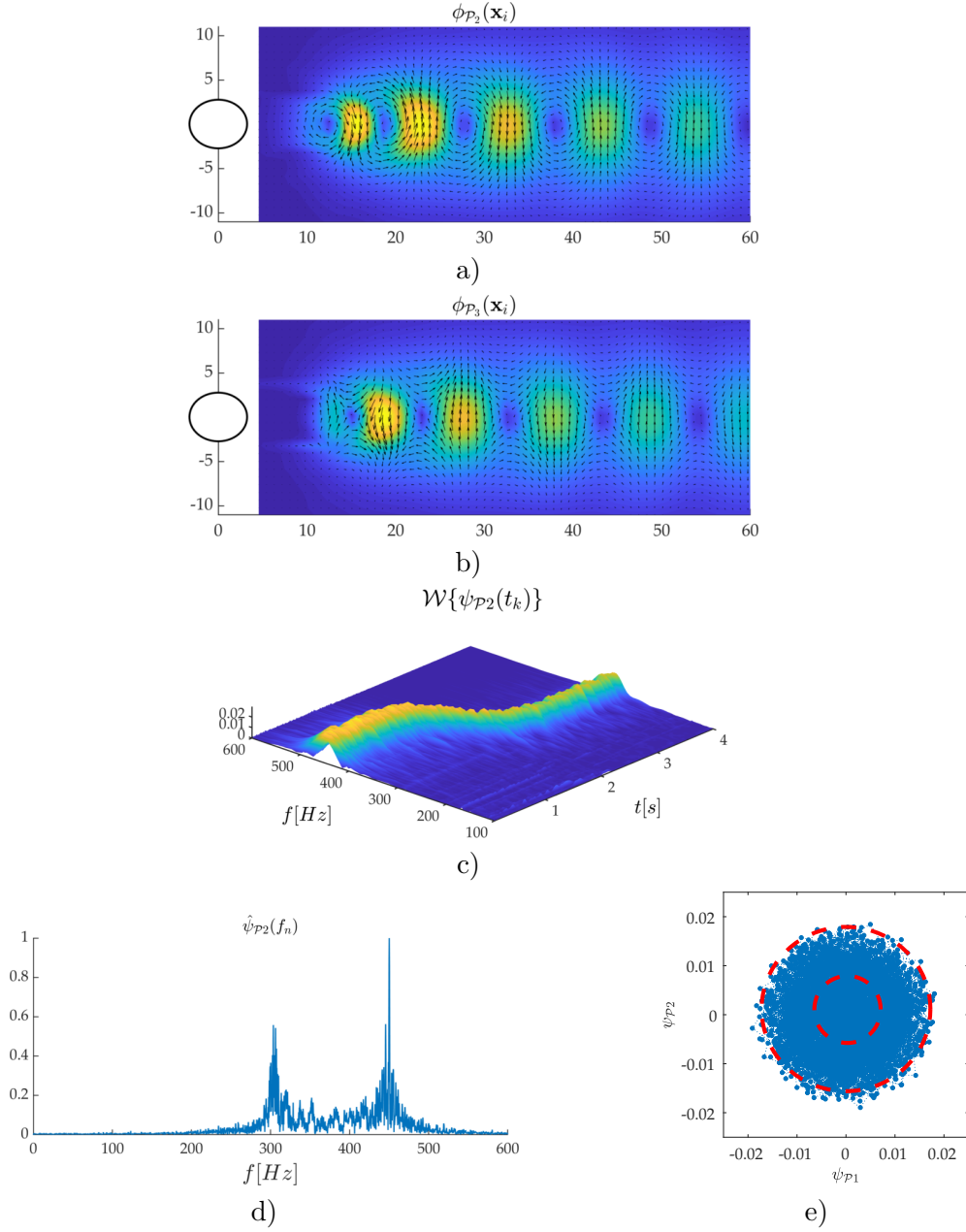


Figure 13: Second and third POD modes for the transient case. Figure structured as Figure 5.

map of the modulus of the Fourier transformed transfer function \hat{K} while Figure 14b) shows its diagonal together with the filter transfer function used to identify the scales. The dataset is partitioned into six scales:

Scale	$\mathcal{H}_{\mathcal{L}}$	\mathcal{H}_1	\mathcal{H}_2	\mathcal{H}_3	\mathcal{H}_4	\mathcal{H}_5	
$ \mathcal{H}_n \approx 1 \forall f \in$	$[0, 10]$	$[10, 290]$	$[290, 320]$	$[320, 430]$	$[430, 470]$	$[470, 1500]$	H_z

The first scale is focused on the slow variation of the flow, identified by the low pass filter $\mathcal{H}_{\mathcal{L}}$. The third scale, \mathcal{H}_2 , is centered around the first peak, while the fifth scale, \mathcal{H}_4 , is centered around the second peak. Scales \mathcal{H}_1 , \mathcal{H}_3 and \mathcal{H}_5 cover the remaining portions of the spectrum.

The spatial structure and the temporal evolution of the first mPOD modes are shown in Figure 15. This mode is analogous to the first POD mode in Figure 12, with a smoother temporal evolution as its frequency content is bounded to $f < 10Hz$. The remaining mPOD

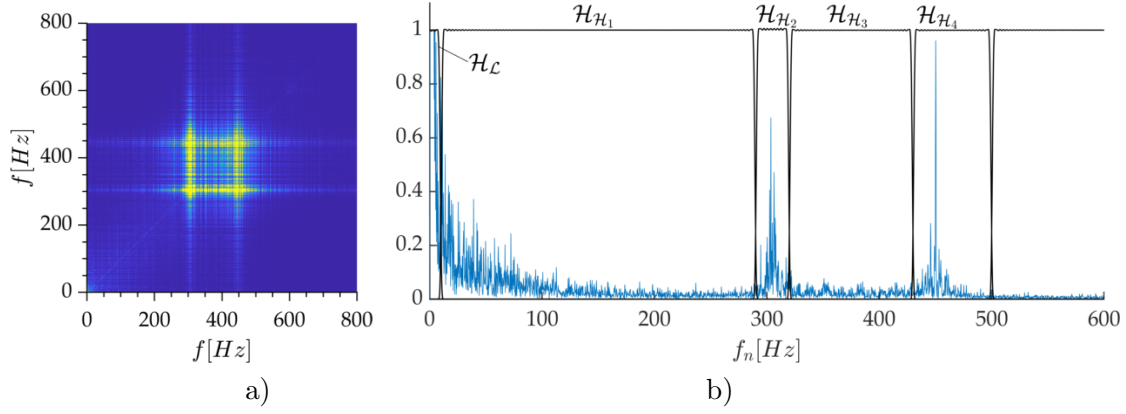


Figure 14: Same as Figure 6, but for the transient test case. The spectrum is divided into six scales. H_L is associated with the large scale variation of the flow, H_{H2} and H_{H4} with the vortex shedding in the two steady states, while the remaining scales cover the intermediate and high frequency portions.

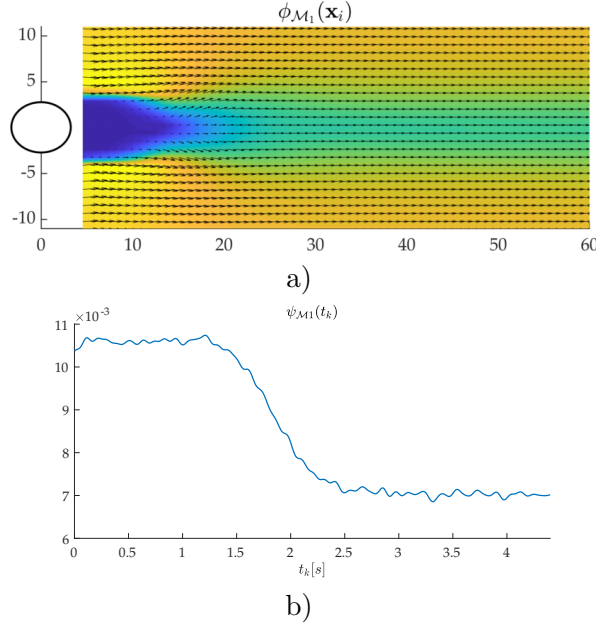


Figure 15: Spatial structure (a) and temporal structure (b) of the dominant mPOD mode for the transient test case.

modes, obtained in pairs of equal energy, are shown in Figures 16, 17, and 18, keeping the usual structure of the figure as in the previous subsection.

The first pair of modes in Figure 16 is associated to the first stationary condition, with no significant contribution appearing outside the spectral bandwidth that characterizes the first vortex shedding. Interestingly, this mode has also no appreciable contribution for $t > 1.5s$, as shown by the CWT of its temporal structure in 16c): while the filters bound the spectral constraints of the mode, the diagonalization of the correlation matrix at each of the corresponding scales also allows for temporal localization. The associated spatial structures resemble more closely the ones observed in the stationary test case investigated in the previous section (see Figure 7a). Similarly, the second pair of modes in Figure 17 captures the vortex shedding in the second steady-state condition, while Figure 18 allows analyzing the modes associated with the flow transient.

To conclude, Figure 19 shows the decomposition convergence for the POD, the DFT, and

the mPOD for the transient test case. Recalling that for this dataset the temporal average has not been removed, the decomposition convergence starts in the DFT from $\mathcal{E}_{\mathcal{F}}(1) = 18.7\%$ — that is the temporal average accounts for 81.3% of the convergence. Since the spectrum has been here partitioned more than in the previous case, the loss of decomposition convergence of the mPOD over the POD is here slightly more pronounced. The information in the first three POD modes is now distributed over the first seven mPOD modes. Nevertheless, the mPOD allows for much better convergence than the DFT while enabling localization both in the frequency and in the time domain and hence— through a projection of the data— in space.

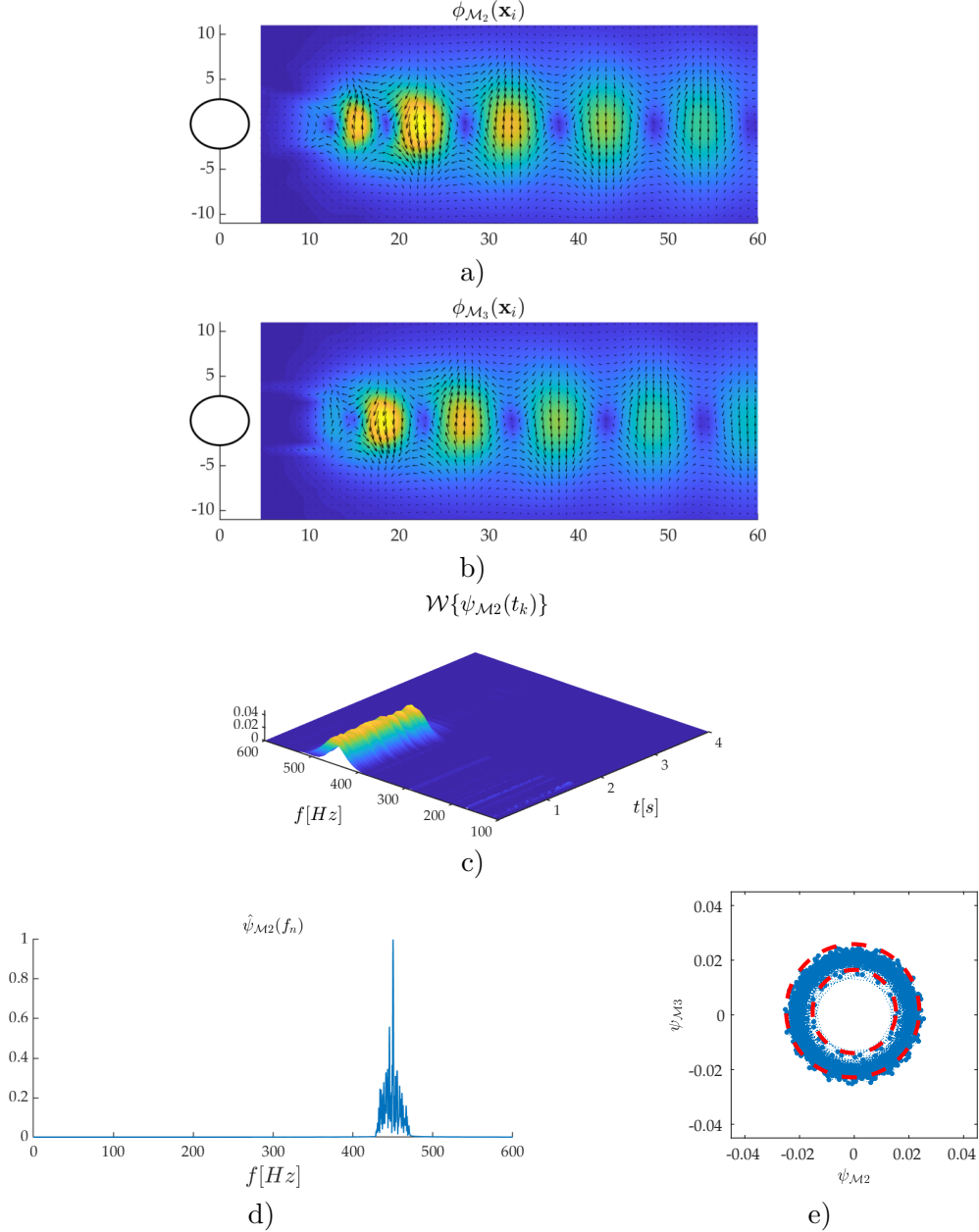


Figure 16: Same as Figure 13, but for the second and third mPOD modes.

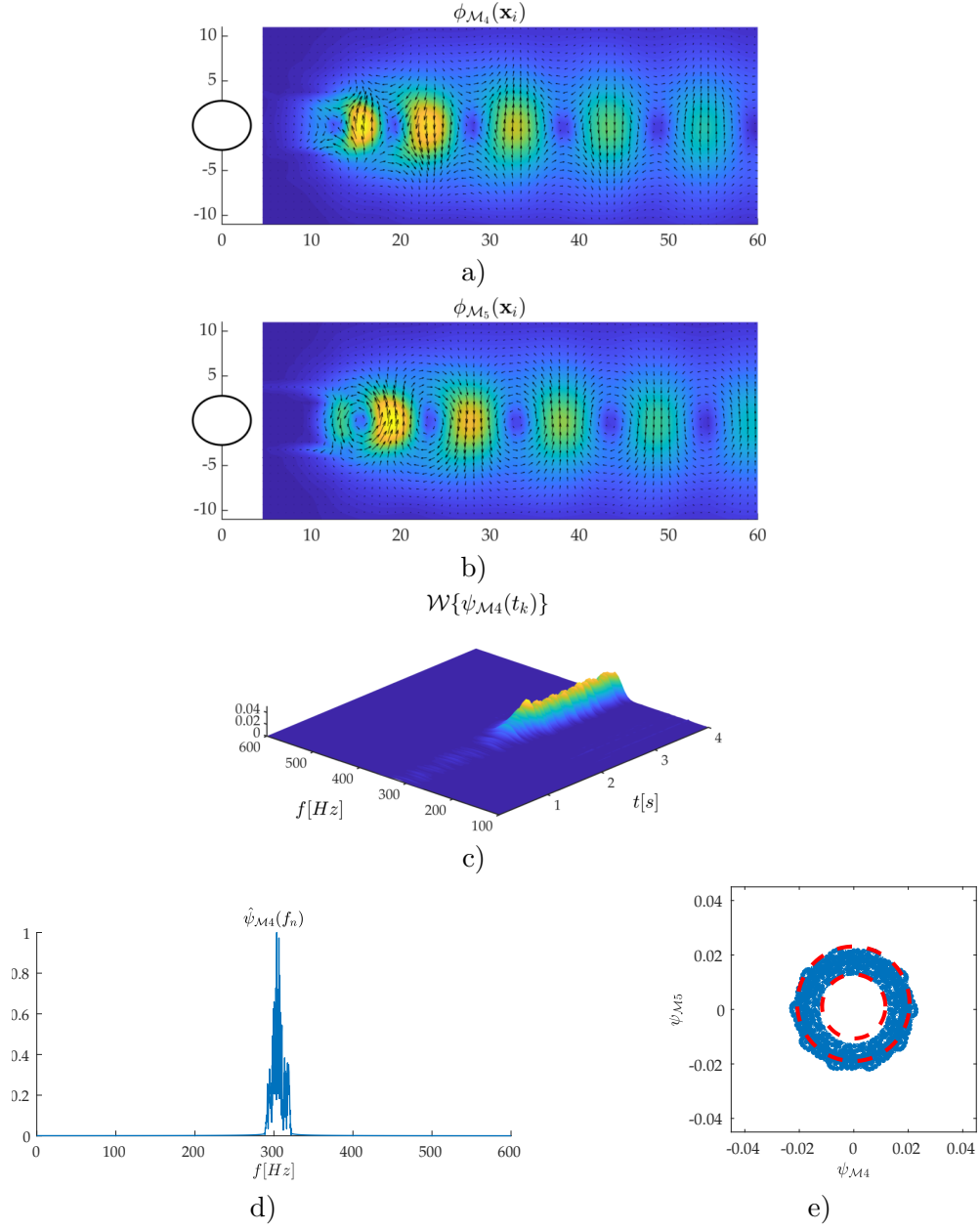


Figure 17: Same as Figure 13, but for the fourth and fifth mPOD modes.

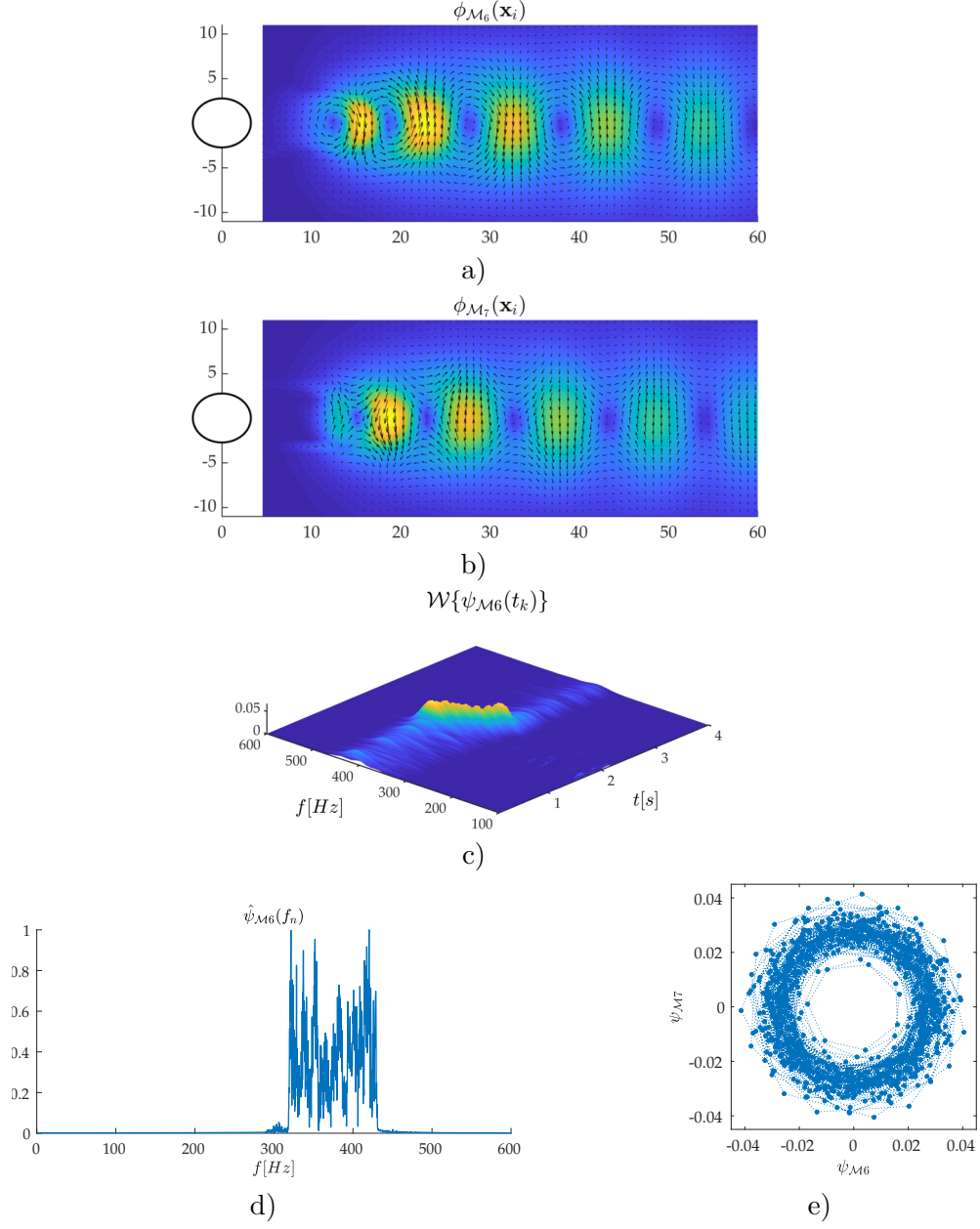


Figure 18: Same as Figure 13, but for the sixth and seventh mPOD modes.

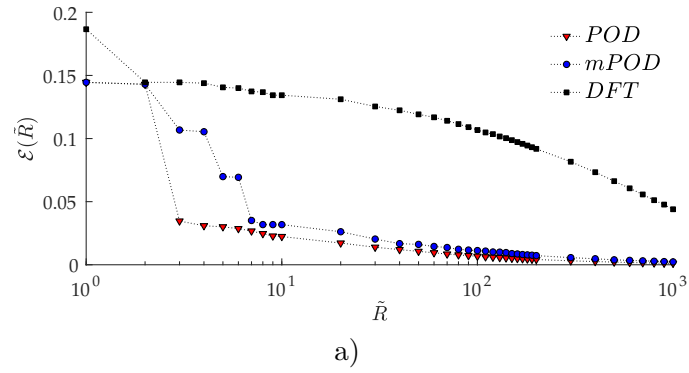


Figure 19: Decomposition error \mathcal{E} in (2) as a function of the number of modes included in the summation (1) for the POD, the mPOD and the DFT of the transient test case.

5 Conclusions and Outlook

A brief review of data-driven decompositions was presented, including the recently developed Multiscale Proper Orthogonal Decomposition (mPOD). This decomposition blends Multiresolution Analysis (MRA) and POD, generalizing POD and DMD in a single formulation, which combines the energy optimality of the first and the spectral purity of the second. The Multiscale Proper Orthogonal Decomposition (mPOD) has been tested on Time-Resolved PIV measurements of the flow past a cylinder in stationary and in transitory conditions.

In stationary conditions, the dataset consists of 4000 snapshots sampled at a frequency of $3kHz$ over an observation time of $1.33s$. The free stream velocity is kept constant at $U_\infty = 12.1m/s$ producing the canonical von Karman vortex shedding at a frequency of $f_d \approx 450Hz$. While the DMD algorithm correctly identifies the dominant frequency of the vortex shedding, the standard implementation does not converge to the dataset as all the computed modes vanish within a small fraction of the observation time. The DFT, on the other hand, allows detecting the dominant harmonic modes while still ensuring convergence, which is nevertheless rather poor and requires about 1000 modes to reach a decomposition error of approximately $\mathcal{E} \approx 20\%$. On the other extreme, such decomposition error is reached by the POD using only three modes. These capture the overall spatial structures of the vortex shedding and reveal an amplitude modulation whose energy content is scattered across the whole range of discrete frequencies. The mPOD proved capable of separating the two sources of such modulation, namely the contribution of harmonic phenomena evolving at a similar frequency, most probably linked to three-dimensional effects on the wake flows, from those linked to other contributions with a broader spectrum. This result is achieved while ensuring a decomposition convergence comparable to the POD, with 7 modes sufficient to have a decomposition error of $\mathcal{E} \approx 20\%$.

In the transient conditions, the dataset consists of 13500 snapshots sampled over an observation time of $4.5s$. The free stream velocity is varied from $U_\infty = 12.1m/s$ to $U_\infty = 7.9m/s$, producing a change of frequency in the vortex shedding from $f_d \approx 450Hz$ to $f_d \approx 300Hz$. Because of the nonlinearity of such transitory, the DMD is unable to detect the relevant frequencies and to converge to the dataset. While the DFT is able to identify the shedding frequencies and to converge to the data (yet requiring 1230 modes to achieve $\mathcal{E} \approx 20\%$), no time localization is possible due to the infinite duration of its basis.

The optimal convergence of the POD results in the opposite problem, with only three modes describing the entire dataset and producing $\mathcal{E}_P \approx 3.4\%$. This is achieved at the cost of assigning to a single mode (and its phase-shifted counterpart) the whole evolution of the vortex shedding. The corresponding spatial structures are consequently a mix of features from these different phases of the flow evolution, which becomes indistinguishable. The spectral constraints of the mPOD allow for distinguishing the various steps in the evolution of the dataset both in the time and the frequency domains, assigning different modes accordingly. Thanks to the MRA architecture, this is achieved with a minor loss in the decomposition convergence with respect to the optimal POD, with only 7 mPOD modes required to achieve $\mathcal{E} \approx 4\%$.

In conclusion, the results prove the enhanced feature detection capabilities of the mPOD on TR-PIV datasets and the significant enhancement advantages of combining energy optimality and spectral constraints. Future works are now aimed at testing different forms of MRA on the resulting mPOD, in implementing methods for the objective definition of the MRA scales and in developing a faster algorithm that hinges on the sparsity of the correlation matrices of each scale in the frequency domain.

Acknowledgements

The authors gratefully acknowledge an insightful discussion on the cylinder wake flow with Prof. Bernd Noack.

References

- Christian Amor, José M. Pérez, Philipp Schlatter, Ricardo Vinuesa, and Soledad Le Clainche. Soft computing techniques to analyze the turbulent wake of a wall-mounted square cylinder. In *Advances in Intelligent Systems and Computing*, pages 577–586. Springer International Publishing, may 2019. doi: 10.1007/978-3-030-20055-8_55.
- Nadine Aubry, Régis Guyonnet, and Ricardo Lima. Spatiotemporal analysis of complex signals: Theory and applications. *Journal of Statistical Physics*, 64(3-4):683–739, aug 1991. doi: 10.1007/bf01048312.
- Peter Benner, Serkan Gugercin, and Karen Willcox. A survey of projection-based model reduction methods for parametric dynamical systems. *SIAM Review*, 57(4):483–531, jan 2015. doi: 10.1137/130932715.
- Zachary P. Berger, Patrick R. Shea, Matthew G. Berry, Bernd R. Noack, Sivaram Gogineni, and Mark N. Glauser. Active flow control for high speed jets with large window PIV. *Flow, Turbulence and Combustion*, 94(1):97–123, nov 2014. doi: 10.1007/s10494-014-9580-2.
- M. Bergmann and L. Cordier. Optimal control of the cylinder wake in the laminar regime by trust-region methods and POD reduced-order models. *Journal of Computational Physics*, 227(16):7813–7840, aug 2008. doi: 10.1016/j.jcp.2008.04.034.
- G Berkooz, P Holmes, and J L Lumley. The proper orthogonal decomposition in the analysis of turbulent flows. *Annual Review of Fluid Mechanics*, 25(1):539–575, jan 1993. doi: 10.1146/annurev.fl.25.010193.002543.
- Christopher M. Bishop. *Pattern Recognition and Machine Learning*. Springer New York, 2011. ISBN 0387310738.
- J. A. Bourgeois, B. R. Noack, and R. J. Martinuzzi. Generalized phase average with applications to sensor-based flow estimation of the wall-mounted square cylinder wake. *Journal of Fluid Mechanics*, 736:316–350, nov 2013. doi: 10.1017/jfm.2013.494.
- Steven L. Brunton and Bernd R. Noack. Closed-loop turbulence control: Progress and challenges. *Applied Mechanics Reviews*, 67(5):050801, aug 2015. doi: 10.1115/1.4031175.
- A. Cammilleri, F. Gueniat, J. Carlier, L. Pastur, E. Memin, F. Lusseyran, and G. Artana. POD-spectral decomposition for fluid flow analysis and model reduction. *Theor. Comput. Fluid Dyn.*, 27(6):787–815, feb 2013. doi: 10.1007/s00162-013-0293-2.
- J. G. Chen, Y. Zhou, R. A. Antonia, and T. M. Zhou. Characteristics of the turbulent energy dissipation rate in a cylinder wake. *Journal of Fluid Mechanics*, 835:271–300, nov 2017. doi: 10.1017/jfm.2017.765.
- Kevin K. Chen, Jonathan H. Tu, and Clarence W. Rowley. Variants of dynamic mode decomposition: Boundary condition, koopman, and fourier analyses. *Journal of Nonlinear Science*, 22(6):887–915, apr 2012. doi: 10.1007/s00332-012-9130-9.
- J. H. Citriniti and W. K. George. Reconstruction of the global velocity field in the axisymmetric mixing layer utilizing the proper orthogonal decomposition. *Journal of Fluid Mechanics*, 418: 137–166, sep 2000. doi: 10.1017/s0022112000001087.
- F. G. Ergin, B.B. Watz, K. Erglis, and A. Cebers. Modal analysis of magnetic microconvection. *Magnetohydrodynamics*, 50(4):339–352, 2014.

- Meyer Knud Erik, Cavar Dalibor, and Pedersen Jakob M. Pod as tool for comparison of piv and les data. In *7th International Symposium on Particle Image Velocimetry*, Rome, Italy, September 2007.
- M. Ghil. Advanced spectral methods for climatic time series. *Reviews of Geophysics*, 40(1), 2002. doi: 10.1029/2000rg000092.
- A Gronsksis, J D Adamo, A Cammilleri, and G Artana. Reduced order models for wake control with a spinning cylinder. *Journal of Physics: Conference Series*, 166:012016, may 2009. doi: 10.1088/1742-6596/166/1/012016.
- A. Hannachi, I. T. Jolliffe, and D. B. Stephenson. Empirical orthogonal functions and related techniques in atmospheric science: A review. *International Journal of Climatology*, 27(9): 1119–1152, 2007. doi: 10.1002/joc.1499.
- F.J. Harris. On the use of windows for harmonic analysis with the discrete fourier transform. *Proceedings of the IEEE*, 66(1):51–83, 1978. doi: 10.1109/proc.1978.10837.
- K. Hasselmann. PIPs and POPs: The reduction of complex dynamical systems using principal interaction and oscillation patterns. *Journal of Geophysical Research*, 93(D9):11015, 1988. doi: 10.1029/jd093id09p11015.
- P. J. Holmes, J. L. Lumley, G. Berkooz, J. C. Mattingly, and R. W. Wittenberg. Low-dimensional models of coherent structures in turbulence. *Phys. Rep.*, 287(4):337–384, aug 1997. doi: 10.1016/s0370-1573(97)00017-3.
- Philip Holmes, John L. Lumley, and Gal Berkooz. *Turbulence, Coherent Structures, Dynamical Systems and Symmetry*. Cambridge University Press, 1996. doi: 10.1017/cbo9780511622700.
- J. F. Huang, Y. Zhou, and T. Zhou. Three-dimensional wake structure measurement using a modified PIV technique. *Experiments in Fluids*, 40(6):884–896, may 2006. doi: 10.1007/s00348-006-0126-9.
- A. K. M. Fazle Hussain and M. Hayakawa. Eduction of large-scale organized structures in a turbulent plane wake. *Journal of Fluid Mechanics*, 180(-1):193, jul 1987. doi: 10.1017/s0022112087001782.
- J. N. Kutz, X. Fu, and S. L. Brunton. Multiresolution dynamic mode decomposition. *SIAM J. Appl. Dyn. Syst.*, 15(2):713–735, jan 2016. doi: 10.1137/15m1023543.
- John L. Lumley. *Stochastic Tools in Turbulence*. DOVER PUBN INC, 1970. ISBN 0486462706.
- John L. Lumley and Andrew Poje. Low-dimensional models for flows with density fluctuations. *Physics of Fluids*, 9(7):2023–2031, jul 1997. doi: 10.1063/1.869321.
- S.G. Mallat. *A Wavelet Tour of Signal Processing*. Elsevier LTD, Oxford, 2009. ISBN 0123743702.
- S. Maurel, J. Borée1, and J.L. Lumley2. Extended proper orthogonal decomposition: Application to jet/vortex interaction. *Flow, Turbulence and Combustion*, 67(2):125–136, 2001. doi: 10.1023/a:1014050204350.
- M. A. Mendez, M. Balabane, and J.-M Buchlin. Multi-scale proper orthogonal decomposition (mPOD). In *AIP Conference Proceedings*, 2018a. doi: 10.1063/1.5043720.
- M. A. Mendez, M.T. Scelzo, and J.-M. Buchlin. Multiscale modal analysis of an oscillating impinging gas jet. *Experimental Thermal and Fluid Science*, 91:256–276, feb 2018b. doi: 10.1016/j.expthermflusci.2017.10.032.

- M. A. Mendez, M. Balabane, and J.-M. Buchlin. Multi-scale proper orthogonal decomposition of complex fluid flows. *Journal of Fluid Mechanics*, 870:988–1036. Preprint available at <https://arxiv.org/abs/1804.09646>, may 2019. doi: 10.1017/jfm.2019.212.
- M.A. Mendez, M. Raiola, A. Masullo, S. Discetti, A. Ianiro, R. Theunissen, and J.-M. Buchlin. POD-based background removal for particle image velocimetry. *Experimental Thermal and Fluid Science*, 80:181–192, jan 2017. doi: 10.1016/j.expthermflusci.2016.08.021.
- Michel Misiti, Yves Misiti, Georges Oppenheim, and Jean-Michel Poggi. *Wavelet Toolbox User’s Guide*. Mathworks, 2015.
- Takaaki Murata, Kai Fukami, and Koji Fukagata. Nonlinear mode decomposition with convolutional neural networks for fluid dynamics. *Journal of Fluid Mechanics*, 882, nov 2019. doi: 10.1017/jfm.2019.822.
- Davide Ninni and Miguel Alfonso Mendez. Modulo: A software for multiscale proper orthogonal decomposition of data. *in Preparation*, 2020. Codes available at <https://github.com/mendezVKI/MODULO>. Accessed: 2019-11-22.
- B. R. Noack, W. Stankiewicz, M. Morzyński, and P. J. Schmid. Recursive dynamic mode decomposition of transient and post-transient wake flows. *J. Fluid Mech.*, 809:843–872, nov 2016. doi: 10.1017/jfm.2016.678.
- Bernd R. Noack. From snapshots to modal expansions – bridging low residuals and pure frequencies. *J. Fluid Mech.*, 802:1–4, aug 2016. doi: 10.1017/jfm.2016.416.
- Bernd R. Noack, Konstantin Afanasiev, Marek Morzyński, Gilead Tadmor, and Frank Thiele. A hierarchy of low-dimensional models for the transient and post-transient cylinder wake. *Journal of Fluid Mechanics*, 497:335–363, dec 2003. doi: 10.1017/s0022112003006694.
- S. Pawar, S. M. Rahman, H. Vaddireddy, O. San, A. Rasheed, and P. Vedula. A deep learning enabler for nonintrusive reduced order modeling of fluid flows. *Physics of Fluids*, 31(8):085101, aug 2019. doi: 10.1063/1.5113494.
- Cécile Penland and Theresa Magorian. Prediction of niño 3 sea surface temperatures using linear inverse modeling. *Journal of Climate*, 6(6):1067–1076, 1993. doi: 10.1175/1520-0442(1993)006<1067:PONSST>2.0.CO;2.
- Cécile Penland. A stochastic model of IndoPacific sea surface temperature anomalies. *Physica D: Nonlinear Phenomena*, 98(2-4):534–558, nov 1996. doi: 10.1016/0167-2789(96)00124-8.
- Per Petersson, Rikard Wellander, Jimmy Olofsson, Henning Carlsson, Christian Carlsson, Bo Beltoft Watz, Nicolas Boetkjaer, Mattias Richter, Marcus Aldén, Laszlo Fuchs, and Xue-Song Bai. Simultaneous high-speed piv and oh plif measurements and modal analysis for investigating flame-flow interaction in a low swirl flame. In *16th In Symp on Applications of Laser Techniques to Fluid Mechanics*, Lisbon, Portugal, July 2012.
- Jean Rabault, Miroslav Kuchta, Atle Jensen, Ulysse Réglade, and Nicolas Cerardi. Artificial neural networks trained through deep reinforcement learning discover control strategies for active flow control. *Journal of Fluid Mechanics*, 865:281–302, feb 2019. doi: 10.1017/jfm.2019.62.
- Marco Raiola, Stefano Discetti, and Andrea Ianiro. On PIV random error minimization with optimal POD-based low-order reconstruction. *Experiments in Fluids*, 56(4), mar 2015. doi: 10.1007/s00348-015-1940-8.
- S. S. Rao. *Mechanical Vibrations*. Pearson, 5th edition, 2010.

- W. C. Reynolds and A. K. M. F. Hussain. The mechanics of an organized wave in turbulent shear flow. part 3. theoretical models and comparisons with experiments. *Journal of Fluid Mechanics*, 54(2):263–288, jul 1972. doi: 10.1017/s0022112072000679.
- C. W. Rowley and S. T.M. Dawson. Model reduction for flow analysis and control. *Annu. Rev. Fluid Mech.*, 49(1):387–417, jan 2017. doi: 10.1146/annurev-fluid-010816-060042.
- Clarence W. Rowley, Tim Colonius, and Richard M. Murray. Model reduction for compressible flows using POD and galerkin projection. *Physica D: Nonlinear Phenomena*, 189(1-2):115–129, feb 2004. doi: 10.1016/j.physd.2003.03.001.
- C.W. Rowley, I. Mezić, S. Bagheri, P. Schlatter, and D.S. Henningson. Spectral analysis of nonlinear flows. *J. Fluid Mech.*, 641:115, nov 2009. doi: 10.1017/s0022112009992059.
- P.J. Schmid. Dynamic mode decomposition of numerical and experimental data. *J. Fluid Mech.*, 656:5–28, jul 2010. doi: 10.1017/s0022112010001217.
- Moritz Sieber, C. Oliver Paschereit, and Kilian Oberleithner. Spectral proper orthogonal decomposition. *J Fluid Mech*, 792:798–828, mar 2016. doi: 10.1017/jfm.2016.103.
- Stefan G. Siegel, Jorgen Seidel, Casey Fagley, D. M. Luchtenburg, Kelly Cohen, and Thomas Mclaughlin. Low-dimensional modelling of a transient cylinder wake using double proper orthogonal decomposition. *Journal of Fluid Mechanics*, 610:1–42, aug 2008. doi: 10.1017/s0022112008002115.
- L. Sirovich. Turbulence and the dynamics of coherent structures: Part i. coherent structures. *Quart. Appl. Math*, 45(3):561–571, 1987. doi: <https://doi.org/10.1090/qam/910462>.
- L. Sirovich. Chaotic dynamics of coherent structures. *Physica D*, 37(1):126–145, 1989. doi: [https://doi.org/10.1016/0167-2789\(89\)90123-1](https://doi.org/10.1016/0167-2789(89)90123-1).
- Julius O. Smith. *Mathematics of the Discrete Fourier Transform (DFT): with Audio Applications*. W3K Publishing; 2 edition, April 2007. ISBN 978-0974560748.
- J Sung and J Y Yoo. Three-dimensional phase averaging of time-resolved PIV measurement data. *Measurement Science and Technology*, 12(6):655–662, may 2001. doi: 10.1088/0957-0233/12/6/301.
- Gilead Tadmor, Oliver Lehmann, Bernd R. Noack, and Marek Morzyński. Mean field representation of the natural and actuated cylinder wake. *Physics of Fluids*, 22(3):034102, mar 2010. doi: 10.1063/1.3298960.
- K. Taira, S. L. Brunton, S. T. M. Dawson, C. W. Rowley, T. Colonius, B. J. McKeon, O. T. Schmidt, S. Gordeyev, V. Theofilis, and L. S. Ukeiley. Modal analysis of fluid flows: An overview. *AIAA J.*, 55(12):4013–4041, dec 2017. doi: 10.2514/1.j056060.
- Raf Theunissen. *Adaptive resolution in PIV image analysis - Application to complex flows and interfaces*. PhD thesis, von Karman Institute for Fluid Dynamics & Technische Universiteit Delft, The Netherlands & Vrije Universiteit Brussel, Belgium,, 2010.
- Aaron Towne, Oliver T. Schmidt, and Tim Colonius. Spectral proper orthogonal decomposition and its relationship to dynamic mode decomposition and resolvent analysis. *Journal of Fluid Mechanics*, 847:821–867, may 2018. doi: 10.1017/jfm.2018.283.
- Jonathan H. Tu, Clarence W. Rowley, Dirk M. Luchtenburg, Steven L. Brunton, and J. Nathan Kutz. On dynamic mode decomposition: Theory and applications. *Journal of Computational Dynamics*, 1(2):391–421, dec 2014. doi: 10.3934/jcd.2014.1.391.

- Václav Uruba. Decomposition methods in turbulence research. *EPJ Web of Conferences*, 25: 01095, 2012. doi: 10.1051/epjconf/20122501095.
- Václav Uruba. Near wake dynamics around a vibrating airfoil by means of PIV and oscillation pattern decomposition at reynolds number of 65 000. *Journal of Fluids and Structures*, 55: 372–383, may 2015. doi: 10.1016/j.jfluidstructs.2015.03.011.
- Václav Uruba and Pavel Procházka. On interpretation of spatiotemporal data decomposition. In *15th International Conference on Fluid Control, Measurements and Visualization*, 2019.
- Hans von Storch and Jinsong Xu. Principal oscillation pattern analysis of the 30- to 60-day oscillation in the tropical troposphere. *Climate Dynamics*, 4(3):175–190, sep 1990. doi: 10.1007/bf00209520.
- P. Welch. The use of fast fourier transform for the estimation of power spectra: A method based on time averaging over short, modified periodograms. *IEEE Transactions on Audio and Electroacoustics*, 15(2):70–73, jun 1967. doi: 10.1109/tau.1967.1161901.
- Jerry Westerweel and Fulvio Scarano. Universal outlier detection for PIV data. *Experiments in Fluids*, 39(6):1096–1100, aug 2005. doi: 10.1007/s00348-005-0016-6.
- C H K Williamson. Vortex dynamics in the cylinder wake. *Annual Review of Fluid Mechanics*, 28(1):477–539, jan 1996. doi: 10.1146/annurev.fl.28.010196.002401.
- J. Wu, J. Sheridan, M. C. Welsh, and K. Hourigan. Three-dimensional vortex structures in a cylinder wake. *Journal of Fluid Mechanics*, 312:201–222, apr 1996. doi: 10.1017/s0022112096001978.
- H. J. Zhang, Y. Zhou, and R. A. Antonia. Longitudinal and spanwise vortical structures in a turbulent near wake. *Physics of Fluids*, 12(11):2954, 2000. doi: 10.1063/1.1309532.
- T. Zhou, Y. Zhou, M. W. Yiu, and L. P. Chua. Three-dimensional vorticity in a turbulent cylinder wake. *Experiments in Fluids*, 35(5):459–471, nov 2003. doi: 10.1007/s00348-003-0700-3.